Drug Delivery and Translational Research
https://doi.org/10.1007/s13346-026-02124-7

ORIGINAL ARTICLE

Accelerating wound healing rates with *Cucurbita pepo* leaf extract loaded electrospun poly(methyl methacrylate)/Halloysite/Chitosan/$CaCO_3$ composite nanofibers through in vitro and in vivo assessments

Esraa B. Abdelazim[1] · Shaza H. Aly[2] · Shahira H. EL-Moslamy[3] · Hend H. Mohamed[1] · Enas A. Abdul-Baki[4] · Marwa Mosaad Shakweer[5,6] · Noura G. Eissa[1,7] · Elbadawy A. Kamoun[8,9] · Mahmoud Elsabahy[1,10] · Samar A. Salim[11]

Received: 18 January 2026 / Accepted: 11 April 2026
© The Author(s) 2026

Abstract

Cucurbita pepo leaf extract (CPE) was incorporated into electrospun poly(methyl methacrylate)/ halloysite/chitosan/$CaCO_3$ (PMMA/Hal/CS/$CaCO_3$) composite nanofibers to develop a novel biomaterial for accelerating wound healing rates. The different nanofibrous scaffolds were successfully fabricated and characterized through scanning electron microscopy (SEM), Fourier-transform infrared spectroscopy (FTIR), and X-ray diffraction (XRD). SEM analysis revealed uniform, smooth nanofibers, while FTIR and XRD confirmed the integration of CPE into nanofiber matrix, indicating an amorphous structure and effective dispersion of the extract. In vitro agar well-diffusion and antibiofilm assays revealed that the optimized formulation exhibited potent antimicrobial activity against wound-associated pathogens. The nanofibers composite based on PMMA provides structural stability, while Hal enhances mechanical properties and cell adhesion. Additionally, CS contributes to biodegradability and moisture retention, both of which are essential for effective wound healing. Furthermore, the inclusion of CPE offers additional antimicrobial benefits, further promoting the wound healing process. In vivo studies confirmed the wound-healing potential of the optimal loaded scaffold, with a 99.9% healing rate achieved by day 14. In vivo studies further demonstrated that CPE-loaded nanofibers significantly enhanced wound closure compared to untreated controls, likely due to the synergistic effects between CPE and PMMA/Hal/CS/$CaCO_3$ matrix. Histological analysis revealed increased macrophage infiltration, neovascularization, and fibroblast proliferation by day 7. Overall, these findings underscore the potential of incorporating natural bioactive compounds into electrospun nanofibers to develop biocompatible, eco-friendly antimicrobial materials for advanced wound-healing applications.

✉ Elbadawy A. Kamoun
ekamoun@kfu.edu.sa

✉ Mahmoud Elsabahy
mahmoud.elsabahy@buc.edu.eg

✉ Samar A. Salim
samar.salim@bue.edu.eg

[1] Badr University in Cairo Research Center, Badr University in Cairo, Badr City 11829, Cairo, Egypt

[2] Department of Pharmacognosy, Faculty of Pharmacy, Badr University in Cairo, Badr City 11829, Cairo, Egypt

[3] Bioprocess Development Dep, Genetic Engineering and Biotechnology Research Institute (GEBRI), City of Scientific Research and Technological Applications (SRTA-City), New Borg Al-Arab City 21934, Alexandria, Egypt

[4] Genomic Signature Cancer Center, Next Generation Sequencer Unit, Tanta University Global Educational Hospital, Tanta University, Tanta, Egypt

[5] Department of Pathology, Faculty of Medicine, Badr University in Cairo, Badr City 11829, Cairo, Egypt

[6] Department of Pathology, Faculty of Medicine, Ain Shams University, Cairo, Egypt

[7] Department of Pharmaceutics, Faculty of Pharmacy, Zagazig University, Zagazig 44519, Egypt

[8] Department of Chemistry, College of Science, King Faisal University, 31982 Al-Ahsa, Saudi Arabia

[9] Polymeric Materials Research Dep, Advanced Technology and New Materials Research Institute (ATNMRI), City of Scientific Research and Technological Applications (SRTA-City), New Borg Al-Arab City 21934, Alexandria, Egypt

[10] Pharmaceutics Department, Faculty of Pharmacy, Assiut University, Assiut 71526, Egypt

[11] Nanotechnology Research Center (NTRC), The British University in Egypt (BUE), El-Sherouk City, Cairo 11837, Egypt

Published online: 22 May 2026

Keywords Nanofibers · Electrospinning · Wound healing · Cucurbita pepo · PMMA · Halloysite · Antimicrobial

Introduction

Wound healing is a multifaceted and dynamic process that requires the coordination of several biological and immunological systems to promote tissue regeneration, reduce scar formation, and prevent infection [1–3]. Despite extensive research, impaired wound healing remains a significant healthcare challenge, and conventional therapies available have several drawbacks (*e.g.*, limited skin penetration capacity, unnecessary adhesion to wounds, and potential wound infection) that limit the healing process. Nanoscale materials of different sorts and compositions have been manipulated for wound healing due to their excellent adsorption capacity, drug loading, and antimicrobial properties [4–7]. Among these nanomaterials, nanofibrous materials have emerged as excellent candidates for wound healing and tissue engineering applications [8, 9]. Electrospun nanofibers are ideal platforms for drug delivery applications owing to the possible modifications performed while developing the fibers regarding polymer selection, blending different polymers, and incorporating various natural or synthetic cargoes [10–13]. Components that mimic the extracellular matrix proteins in manufacturing nanofibers are crucial in maintaining cell growth and infiltration, and in enhancing tissue regeneration [14]. Natural or synthetic polymers can be electrospun to produce nanofibrous dressings that offer numerous advantages, such as accelerated healing, reduced side effects, decreased need for aftercare in hospitals and communities, and lower overall treatment costs [15].

Poly(methyl methacrylate) (PMMA) is a transparent, glassy thermoplastic linear polymer characterized by its amorphous and hydrophobic nature, biocompatibility, exceptional mechanical properties, unique optical activity, and favourable processing conditions. The biological inertness of PMMA enabled its use in various biomedical applications [16, 17]. PMMA scaffolds can also be functionalized with bioactive agents such as antimicrobial nanoparticles, growth factors, or extracellular matrix proteins, which enhance their therapeutic efficacy by promoting accelerated healing and minimizing the risk of infection [18]. Recent advancements in the biomedical field have highlighted the potential use of clay minerals in tissue engineering, particularly as enhancers of cell attachment, proliferation, and differentiation [19]. Nano clays and nanoscale aluminosilicates have also contributed to wound repair by promoting hemostatic and anti-inflammatory activities, as well as angiogenesis and re-epithelialization [20]. Chitosan (CS) is a natural biomaterial extensively utilized in the production of wound dressings due to its exceptional biological properties (*e.g.*, biodegradability, bio-adhesiveness, cytocompatibility, and lack of toxicity) [21–24]. Structurally, it is a linear polysaccharide composed of repeating units of *N*-acetylglucosamine, and glucosamine interconnected via $\beta(1–4)$ glycosidic linkages, closely resembling the glycosaminoglycans of extracellular matrices [25].

Calcium ions act as crucial signaling molecules that regulate the migration and proliferation of keratinocytes, facilitating the re-epithelialization process essential for wound closure. Additionally, calcium contributes to the stabilization of the extracellular matrix, promoting structural integrity and supporting effective tissue regeneration during healing [26]. Incorporation of calcium carbonate ($CaCO_3$) within nanofibers might contribute to enhanced cellular adhesion and accelerated wound healing [26].

Medicinal plants and their extracts are considered promising therapeutics for wound healing due to the presence of various active components, such as flavonoids, alkaloids, and terpenoids, as well as their secondary metabolites [27–29]. The therapeutic benefits of these natural extracts can be enhanced when incorporated into nanomaterials. Studies by our group [30] and others [31–34] have demonstrated the enhanced wound-healing capacity of nanofibers loaded with different plant extracts. Numerous plant bioactive compounds have been investigated as potential therapeutic agents for wound healing, reducing inflammation, and mitigating oxidative stress associated with wounds [35, 36].

Cucurbita pepo (*C. pepo)*, known as pumpkin, is classified under the genus *Cucurbita* and the family Cucurbitaceae. *C. pepo* extracts have demonstrated various biological effects, including but not limited to antidiabetic, anti-inflammatory, antihypertensive, antitumor, immunomodulatory, and antibacterial activities [37]. *C. pepo* is a rich source of flavonoids, terpenoids, alkaloids, proteins, lipids, carbohydrates, minerals, and phytosterols [38]. The leaves have been traditionally utilized for their analgesic properties and ability to enhance blood circulation. They were also employed to alleviate biliousness and to cure conditions such as rheumatism, benign prostatic hyperplasia, burns, and wound injuries [38, 39]. The aqueous extract of *C. pepo* leaves exhibited higher percentages of wound contraction and tensile strength, along with a decreased wound healing time and epithelialization, in a wound-healing rat model relative to the control group and the groups that received treatment with povidone-iodine [40]. In the present study, newly designed electrospun PMMA/Hal/CS/$CaCO_3$ nanofibrous scaffolds were loaded with different concentrations of *C. pepo* leaves extract (CPE). The split, characterization, and composition elucidation of CPE were demonstrated,

and the electrospinning process and characterization of the therapeutic nanofibers were illustrated in detail. Moreover, the free and plant extract-loaded nanofibers were evaluated for their in vitro antimicrobic behavior and in vivo wound-healing performance.

Materials and methods

Materials

Polymethyl methacrylate, $M_n \sim 550$ KDa (PMMA) was purchased from Merck (Darmstadt, Germany). Halloysite nano clay (Hal), calcium carbonate ($CaCO_3$), chitosan (CS), $M_n \sim 100$—300 KDa, *N, N*-dimethylformamide (DMF), ≥ 99% reagent grade were gotten from Fisher Chemicals (Hampton, NH). All reagents were utilized as received without any additional purification. Fresh leaves of *Cucurbita pepo* were collected from a private garden located on the Misr Ismailia Road (N 30°17′43.386", E 31°22′27.9804") in Egypt during July 2023. The plant was verified by the taxonomist, Therease Labib, at the El-Orman Botanical Garden in Giza, Egypt. A voucher specimen was deposited with Pharmacognosy Department at Faculty of Pharmacy, Badr University in Cairo (*voucher specimen number: PHG-CP-30*).

The multidrug-resistant human pathogens used in this study were sourced from Bioprocess Development Department at GEBRI, SRTA-City, Egypt. Four *Gram-positive* bacteria (*Bacillus cereus* (ATCC 19637), *Bacillus aureus* (ATCC 25923), *Bacillus epidermidis* (ATCC 14990), and *Bacillus subtilis* (ATCC 11774)) and four *Gram-negative* bacteria (*Salmonella paratyphi* (ATCC 9150), *Pseudomonas aeruginosa* (ATCC 27853), *Escherichia coli* (ATCC 10536), and *Salmonella pneumoniae* (ATCC 10031)) were selected for antimicrobial assay. Four yeast strains, *Candida glabrata* (ATCC 66032), *Candida albicans* (ATCC 10231), *Candida parapsilosis* (ATCC 22019), and *Candida krusei* (ATCC 6258), were also included in the study.

Preparation of CPE

Air-dried leaves of *C. pepo* (100 gm) were extracted with 80% methanol through maceration till exhaustion (1 L × 3). After filtration, the solvent faded away via a rotavapor (Hei-VAP Value, Heidolph) under reduced pressure and at a temperature of 45 °C until dryness, yielding a dried residue (9.73 g). To remove chlorophyll and pigments from the extract, the extract was dissolved in water: methanol (1: 4) and then partitioned successively with n-hexane to yield the hexane fraction (0.88 g), and the remaining defatted total dried extract (8.96 g) was kept in a tightly wrapped bottle at 20 °C for further characterizations [41].

Fabrication of nanofiber scaffolds

Preparation and optimization of nanofiber scaffolds

A PMMA solution (30% *w*/*v*) was prepared by dissolving PMMA in DMF, and the solution was stirred overnight at 500 rpm and 60 °C. Hal was added to the PMMA solution at various concentrations (1, 3, and 5% *w*/*v*) and mixed for 3 h at 500 rpm in room temperature to obtain a homogeneous solution, with Hal being suspended in the solution. Homogeneous PMMA/Hal solutions were fabricated into nanofibers (Table 1) via an electrospinner instrument (MECC, NANON-01A, Japan) to shape the optimal combination and spinning circumstances. The blended mixtures were placed into a 6 mL syringe with a 22G needle. All nanofibers preparation experiments were performed at ambient conditions with a controlled humidity at 45%, while the electrospinning parameters varied, as shown in Table 1. A drum collector covered by aluminum foil was used for the nanofiber deposition. E3 which incorporated the highest concentration of Hal (5%) allowed for the development of uniform nanofibers and was utilized as the optimal PMMA/Hal solution formulation. CPE was added to the optimal PMMA/Hal solution at various concentrations (0.5, 1, 2, and 3% *w*/*v*) to fabricate the extract-loaded nanofibers. After addition, the combination was stirred at 500 rpm for an extra two hours at room temperature until a homogenous PMMA/Hal/CPE blend solution was formed. The blend mixture was electrospun at different parameters (applied voltage 27.5–30 kV, feed rate 0.1–1.3 mL/h, drum speed 1000 rpm, spinneret speed 100, spinneret width 40 mm positioned 15 cm above the collector) (Table 1). CS was weighed in a beaker that had been washed and wet with an acidified aqueous solution. Subsequently, the optimal PMMA/Hal/CPE solution (E5, which incorporated 1% CPE) was added dropwise to the CS baker while continuously stirring, at concentrations of 1% and 3% (w/v). After this addition, the mixture was blended for another two h until a homogenous PMMA/Hal/CPE/CS blend solution was formed. PMMA/Hal/CPE/CS/$CaCO_3$ nanofibers were fabricated by adding $CaCO_3$ at the concentrations of 0.5% and 1% (*w*/*v*) to the optimal PMMA/Hal/CPE/CS solution (E8). All the fabricated nanofibers were stored under vacuum overnight to ensure the complete evaporation of any residual solvent.

Table 1 Optimization of spinning conditions of PMMA/Hal/CPE/CS/$CaCO_3$ nanofiber scaffolds

Formulation No	PMMA (% *w/v*)	Hal (% *w/v*)	CPE (% *w/v*)	CS (% *w/v*)	$CaCO_3$ (% *w/v*)	Voltage (kV)	Feed rate (mL/h)
E1	30%	1%	-	-	-	21	2
E2	30%	3%	-	-	-	22	2
E3	30%	5%	-	-	-	21.5	2
E4	30%	5%	0.5%	-	-	27.5	0.5
E5	30%	5%	1%	-	-	27.5	0.5
E6	30%	5%	2%	-	-	30	0.5
E7	30%	5%	3%	-	-	30	0.2
E8	30%	5%	1%	1%	-	27	1.3
E9	30%	5%	1%	3%	-	30	0.8
E10	30%	5%	1%	1%	0.5%	30	1.9
E11	30%	5%	1%	1%	1%	30	1.3
E12	30%	5%	-	1%	0.5%	28.5	1.3

Characterization of plant extract and fabricated nanofibers

HPLC–MS/MS analysis of CPE

The phytochemical summarizing of the methanol extract of *C. pepo* leaves was performed depending on the available methods [42, 43], utilizing HPLC together with ESI–MS to determine the isolated peak molecular weights. The mass spectra revealing was developed in the ESI range of 100–1000 m/z via *Maslynx 4.1*, and the peaks were characterized by matching their mass spectra and fragmentation patterns with the informed data.

SEM of nanofibers

SEM and EDX (energy-dispersive X-ray spectroscopy) examination were performed utilizing FE-SEM (field emission environmental scanning electron microscope) (Quattro S, Thermo Scientific, USA) to analyse the surface characteristics of the fabricated nanofiber scaffolds. The image analysis was done using *Image J software*.

FT-IR analysis

The chemical configuration of PMMA/Hal/CPE/CS/$CaCO_3$ nanofibers was analysed using (model 8400 s, Shimadzu, Japan). Spectral data were collected over ν ranged of 4000–400 cm^{-1} to acquire distinctive fingerprints and assess the molecular composition of the scaffolds.

X-ray diffraction analysis

XRD outlines of the manufactured nanofibers were gotten via (*Malvern PANalytical*, England, UK) supplemented with Cu Kα radiation. The data were obtained at 2Θ ranging from 5 to 60° with a step size of 0.02 and 0.5 s for each step. The electrospun specimens were mounted on aluminium disks using tape to make sure the samples were flat and correctly positioned.

Swelling study

The scaffolds were cut into (1 × 1 cm) pieces, weighed dry (W_d), and then immersed in 15 ml deionized water at 37 °C for 24 h [44, 45]. At various time intervals (0.25, 0.50, 1.00, 2.00, 4.00, 6.00, 8.00, 24.00 h), excess water was removed using filter paper, and the swollen nanofibers were reweighed (W_e) to track the weight change. Swelling (%) was calculated using Eq. (1).

$$Swelling(\%) = \frac{W_e - W_d}{W_d} \times 100\% \quad (1)$$

Hydrolytic degradation

To estimate the weight loss percentage of different nanofibers in an aqueous environment, each scaffold was cut into 1 × 1 cm pieces and weighed using a sensitive balance [46]. The samples were then immersed in 15 mL of phosphate buffer solution (PBS (pH 7)) and placed in an incubator at

room temperature at various time intervals: (0, 1.0, 1.5, 2.0, 2.5, and 3.0 days). After the specified time, the samples were removed from the buffer, weighed (W_f), and compared to their original dry weight (W_i). The weight loss (%) of each mat was then calculated using Eq. (2).

$$Weight\ loss(\%) = \frac{W_i - W_f}{W_i} \times 100\% \quad (2)$$

Antimicrobial activity of nanofibers

The antimicrobial activities of the nanofibrous scaffolds (E3, E8, E10, E11) were evaluated using the agar-well diffusion manner, spectrophotometric antibiofilm assay, and time-kill kinetics assay. To elucidate the therapeutic benefits of incorporating the plant extract into the nanofibrous scaffolds, the antimicrobial performance of the free CPE (E13) was also investigated.

Agar-well diffusion method

Human pathogens examined were grown in a nutrient broth medium containing 0.5% peptone, 0.3% yeast extract, 0.2% beef extract, and 0.5% NaCl, following the 0.5 McFarland turbidity standards. Microbial cultures (100 µL) were evenly spread on nutrient agar plates using sterile cotton swabs. A sterile cork borer with a diameter of 6 mm was then used to create wells, into which 50 µL of the tested formulations were added. The agar plates were subsequently incubated for 24 h at 37 °C, and the zones of inhibition around each well were measured [47].

Spectrophotometric antibiofilm assay

A microdilution test was used to assess the capacity of the tested formulations to prevent the ability of the tested pathogens to form biofilms [48]. Pathogens were separately inoculated into fresh nutrient broth, incubated at 200 rpm and 37 °C to yield 2×10^5 CFU/mL. Aseptically, 100 µL of each construction was mixed with 900 µL of these planktonic cultures to generate treated cultures. Additionally, untreated (*i.e.*, formulation-free) cultures of the pathogens served as controls. The cultures were then incubated at 200 rpm and 37 °C for a period of 24 h. The spectroscopic measures of microbial turbidity caused by the incubated formulations were determined and the anti-biofilm proportions for each formulation were valued by comparing the optical density of the treated samples to the corresponding controls [49].

Time-kill kinetics assays

This assay was performed for the optimal formulation (E10), which exhibited superior antimicrobial activity in the agar-well diffusion and antibiofilm assays. In this experiment, the macro-broth dilution test was employed [50, 51], where the selected formulation (E10) was applied to each microbial culture's inoculum (5×10^8 CFU/mL). For each pathogen, untreated growth cultures were established as controls. Samples of the pathogens grown at 37 °C and 200 rpm were analyzed at (0, 6, 12, 18, 24, 30, 36, 42, and 48 h). The diluted samples (100 µL) were then swabbed onto nutrient agar dishes. The quantity of visible colonies was calculated and recorded as CFU/mL. The logarithm of the counted colonies (Log_{10} CFU/mL) was then used to quantify the proportion of biofilm reduction of pathogen cells in the treated samples versus the control. A stacked bar plot was used to compare the cell viability of treated and untreated samples at different time points.

In vivo wound healing assay

The in vivo trials were ethically agreed by the Institutional Ethical Committee of Badr University in Cairo, *No. (BUC-IACUC-240623–98)*. Sixteen male Wistar rats weighing 235–255 g were housed in a standard animal house supplied with cages and softwood pellets for bedding at 12-h light/dark life cycle in the room temperature. The rats were randomly divided into four groups, four animals each, anesthetized with ketamine (90 mg/Kg) injection, followed by hair removal before creating wounds on the dorsal surface of each rat skin utilizing a 1 cm^2 biopsy punch [52]. In the treated groups, the wounds were covered with the fabricated nanofibers and fixed with sterile gauze. In the control group, sterile gauze was used to cover the wounds to prevent infection. Group I had no treatment and served as a negative control. Group II was treated with E3 (PMMA/Hal nanofiber) and served as a positive control, Group III was treated with E12 (PMMA/Hal/CS/$CaCO_3$ nanofiber free of the plant extract), and Group IV was treated with the optimal formulation E10 (PMMA/Hal/CPE/CS/$CaCO_3$ nanofiber). After (3, 7, 10, and 14 d), the wound dressings were eliminated, and the diameter of the wounds was determined. The percentage of wound healing was calculated corresponding to *Eq.* (3) [30]:

$$Wound\ healing\% = \frac{A_i - A_d}{A_i} \times 100 \quad (3)$$

A_d and A_i are wound zones on indicated day and day zero, respectively. On day 14, the rats in the groups were sacrificed, and skin samples were immediately placed in 10% formalin which required for histological analysis.

Histological assessment

Biopsies were collected from the wound sites of all studied groups. Specimens were fixed in 10% phosphate-buffered formalin, and 3–5 mm slices were formulated for *H&E* (hematoxylin and Eosin) staining [53]. The degree of wound healing was assessed microscopically as follows:

- Complete wound healing: indicated by whole epithelial closure and complete replacement of granulation tissue by collagen fibers and fibrosis.
- Partial wound healing: indicated by whole epithelial closure and partial replacement of granulation tissue by collagen fibers.
- Delayed wound healing: indicated by partial epithelial closure and failure of replacement of granulation tissue by collagen fibers or focal collagen fiber formation.

Statistical analysis

Values are obtainable as means ± SDs of at least 3 independent trials. One-way investigation of variance (*ANOVA*) with *Tukey–Kramer* multiple comparisons or a two-sided Student's t-test for pairwise evaluations (*GraphPad Prism 6.0, GraphPad*, San Diego, CA) was working to determine the statistical significance of the differences between considered groups. For the antimicrobial assays, the statistical significance was evaluated utilizing one-way analysis of variance (*ANOVA*) and *Tukey's* multiple comparison post hoc test (*MINITAB version 18.1*). Statistical significance was recorded using a 95% confidence interval (p value ≤ 0.05).

Results and discussion

HPLC–ESI–MS/MS of phytoconstituents of CPE

This analysis was used to identify the phytoconstituents in the methanol extract of *C. pepo* leaves. The total ion chromatogram (TIC) in negative (*-ve*) ionization mode is represented in Fig. 1. Fourteen compounds belonging mainly to flavonoids, phenolic acids, and fatty acids have been detected tentatively by comparing their MS characteristics and fragmentation outline (Table 2). Flavonoid glycosides were the primary class of metabolites observed in *C. pepo* methanol extract. Regarding the flavonoids, peak **3** (Luteolin-*O*-hexoside-*O*-deoxyhexoside) showed a deprotonated molecular ion at *m/z* 593 and a fragment ion at 285, corresponding to the loss of hexose and deoxyhexose. Peak **4** has a parent ion peak at *m/z* 593.26 $[M-H]^-$ as well as a daughter ion peak at m/z 285, that corresponds to the removal of deoxyhexosylhexoside and the liberation of kaempferol aglycone. Another kaempferol glycoside was identified as kaempferol-*O*-deoxyhexoside (Afzelin) peak **6** with a deprotonated molecular ion peak at *m/z* 431.16. The apigenin glycosides represented the major flavonoids characterized in *C. pepo* methanol extracts (**5, 7, 8,** and **9**). They tentatively identified as apigenin di-C-hexoside (Vicenin II), apigenin-C-hexoside (Vitexin), apigenin-*O*-hexoside (isovitexin), and apigenin-*O*-deoxyhexoside, respectively. Apigenin has been reported for its therapeutic properties in both acute irritant dermatitis and contact dermatitis models when applied topically, demonstrating potential wound-healing properties [54]. Another investigation documented the involvement of an extract containing apigenin from *Carissa carandas* in wound healing, improving epithelization and tensile strength of the repaired tissue. [55].

This extract was found to enhance wound contraction and increase the tensile strength of wounds in both excision and incision models [55]. Quercetin glycoside is characterized as quercetin-O-malonylhexoside (11) $[M-H]^-$ at *m/z* 549.38 and MS2 at *m/z* 463 (loss of 86 malonyl moiety). Besides, three phenolic acids characterized as caffeic acid derivative (1), caffeoyl-*O*-hexoside (2) and ferulic acid (10) with the ion mass peaks at *m/z* 377.15 $[M-H]^-$ and 401.11 $[M+Na]^+$ for (1), *m/z* 341.14 $[M-H]^-$ for (2), and 193.05 $[M-H]^-$ and 195.05$[M+H]^+$ for (10) for the suggested molecular formulae $C_{18}H_{17}O_9$, $C_{15}H_{18}O_9$, and $C_{10}H_{10}O_4$, respectively. Ferulic acid is a significant component of CPE that facilitates accelerated wound healing in diabetic rats [56]. Ferulic acid-treated wounds were epithelialized more quickly than diabetic wounds and exhibited decreased lipid peroxidation, along with increased superoxide dismutase, catalase, glutathione, serum zinc, nitric oxide, and copper levels [57].

Moreover, three fatty acids identified as trihydroxy-9,14-octadecadienoic acid (12), trihydroxy octadecenoic acid (13), and heptadecadienoic acid isomer (14) appeared at *m/z* 327.27, 329.30, and 265.15, respectively. Eventually, the presence of all bioactive secondary metabolites in the methanol extract of *C. pepo* leaves demonstrate the high potential of the extract to enhance in vivo wound healing. The chemical arrangements of the major characterized compounds are illustrated in Fig. 2.

SEM investigation

SEM images are shown in Fig. 3 of PMMA nanofibers with several weight percentages of Hal, CPE, CS, and $CaCO_3$, confirming the fabrication of nanofibers with accurate

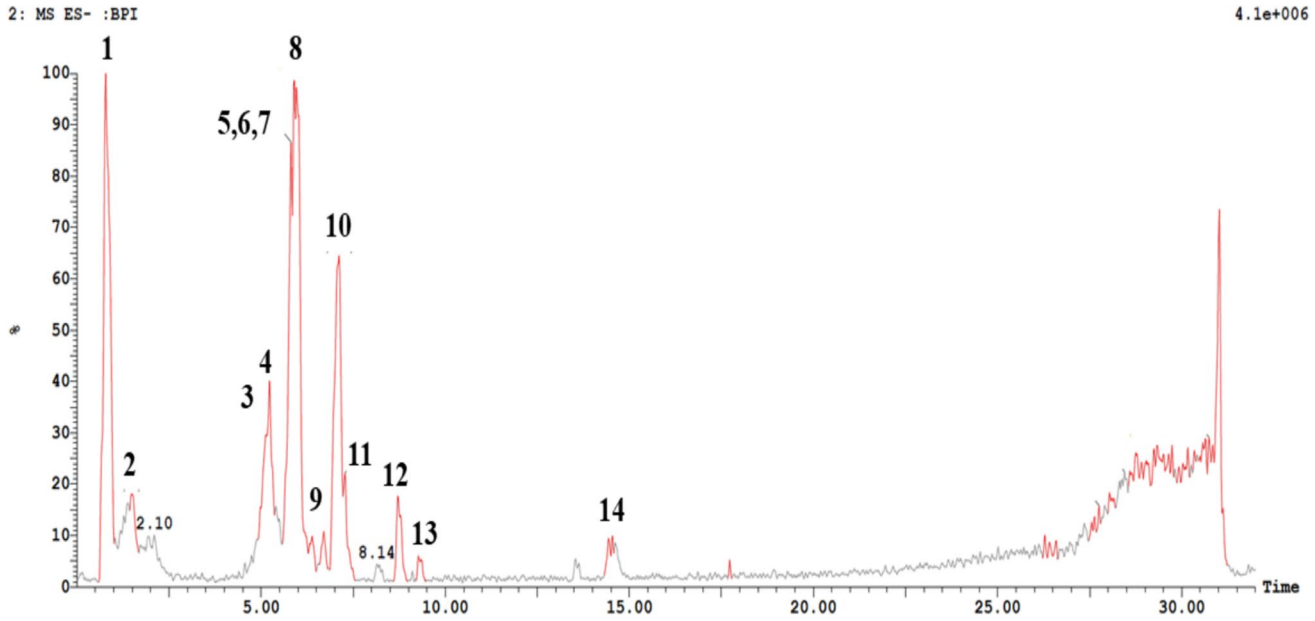

Fig. 1 TIC (Total ion chromatogram) for methanol extract of *C. pepo* leaves in negative positive ionization mode

nanosized diameters. PMMA nanofibers displayed a uniform and smooth morphology with a mean diameter of 0.43 µm ± 0.08 µm (Fig. 3A). The addition of Hal at various concentrations (1–5%) resulted in the formation of fibres of increased thickness, with mean diameters varying from 0.70 ± 0.17 to 0.78 ± 0.20 µm (Figs. 3B-D). Notably, higher Hal concentrations contributed to a more cohesive and interconnected network structure, indicating enhanced uniformity across the fibres. Incorporation of different concentrations of CPE in the nanofibers was accompanied by visible bundling and aggregation within the fibre network (Figs. 3E-G). The mean diameters of the CPE-loaded nanofibers ranged from 0.93 ± 0.35 to 1.02 ± 0.24 µm, with higher concentrations of CPE promoting thicker and more robust fibres. Incorporating 1% CS yielded a compact and well-integrated fibre network with a mean diameter of 0.70 ± 0.12 µm (Fig. 3H). Increasing the CS concentration to 3% (Fig. 3I) resulted in a more pronounced increase in fibre diameter, reaching a mean of 0.92 ± 0.21 µm. The addition of $CaCO_3$ at 0.5% led to a significant increase in fibre diameter, achieving a mean thickness of 1.20 ± 0.31 µm (Fig. 3J). EDX analysis exposed the existence of O, Si, and Al in the nanofibers that incorporated Hal, as shown in Table 3 confirming that no other elements were present in the structure.

FT-IR analysis of CPE-loaded-PMMA/Hal/CS/$CaCO_3$ nanofibers

FT-IR analysis examined possible molecular interactions between the components of the developed nanofibers (*i.e.*, PMMA, Hal, CPE, CS, and $CaCO_3$). Figure 4 illustrates FT-IR spectra of the nanofibers and their components. The main structural components of PMMA are polyethylene chains with methyl and -$OCOCH_3$ groups connected to every second carbon atom. FT-IR spectrum of pure PMMA displayed characteristic absorbance bands as reported previously at 1717 cm^{-1} for C = O in the –$COOCH_3$ group, 1136 cm^{-1} for C–O elongating, ν 1450–1350 cm^{-1} for C–H bending, ν 830 and 747 cm^{-1} for CH_2 rocking, and a broad range between ν 3100–2800 cm^{-1} corresponding to C–H stretching of CH_2 and CH_3 groups [69, 70].

FT-IR spectrum of pure Hal showed well-defined hydroxyl expanding bands at ν 3694, 3624, and 3545 cm^{-1}. The band at ν 3694 cm^{-1} corresponds to the hydroxyl stretching of the inner surface hydroxyl bands. In contrast, the peak at ν 3624 cm^{-1} relates to the out-of-phase vibration of the hydroxyls on the inner surface [71]. The peak detected at ν 3545 cm^{-1} corresponds to the hydrogen linkage between water and the surface of Hal. An additional band is demonstrated at ν 3593 cm^{-1}, resulting from hydrogen bonding between the core of Hal and surrounding water. The shoulder at ν 1121 cm^{-1} corresponds to the stretching mode of apical Si–O, whilst the spectral bands at 1023 and 907 cm^{-1} correspond to the stretching vibrations of Si–O-Si and the twisting modes of Al-O–H. Additional ν 792 and 745 cm^{-1} bands relate to the characteristic OH translation vibrations of Hal [72].

FT-IR spectrum of the CPE consists of bands representing three main functionalities: C = C at ν (1632 cm^{-1}), –OH ν (3288 cm^{-1}), and –C = O ν (1605 cm^{-1}). Additionally, a band is associated with –CH (2923 cm^{-1}) from the polyphenols found in the plant extract [73]. The vibration

Table 2 HPLC–MS/MS identified characteristic phytoconstituents of *Cucurbita pepo* in positive and negative ionization mode

Peak No	Compound name	t_R (min)	Molecular formula	$[M-H]^-/[M+H]^+$ *m/z*	MS^2 fragments	Chemical class	Content%	Ref No
1	Caffeic acid derivative	0.79	$C_{18}H_{17}O_9$	377.15/401.11 $[M+Na]^+$	341	Phenolic acid	20.22	[58]
2	Caffeoyl-*O*-hexoside	1.48	$C_{15}H_{18}O_9$	341.14	179	Phenolic acid	0.75	[59]
3	Luteolin-O-hexoside-O-deoxyhexoside	4.98	$C_{27}H_{30}O_{15}$	593.26	285, 267, 175	Flavonoids	0.27	[60]
4	Kaempferol-O-hexoside-O-deoxyhexoside (Kaempferol-O-robinobioside)	5.12	$C_{27}H_{30}O_{15}$	593.26	285, 227, 151	Flavonoids	2.24	[61]
5	Apigenin di-C-hexoside (Vicenin II)	5.20	$C_{27}H_{30}O_{15}$	593.26/595.23	473, 395, 383, 353, 297	Flavonoids	8.08	[62]
6	kaempferol-O- deoxyhexoside (Afzelin)	5.82	$C_{21}H_{20}O_{10}$	431.16	285, 284, 255, 227	Flavonoids	9.94	[63]
7	Apigenin-8-C-hexoside (Vitexin)	5.90	$C_{21}H_{20}O_{10}$	431.16	341, 311, 269	Flavonoids	7.87	[63]
8	Apigenin-6-C-hexoside (Isovitexin)*	5.95	$C_{21}H_{20}O_{10}$	431.17/433.13	269	Flavonoids	30.49	[64, 65]
9	Apigenin-O-deoxyhexoside	6.39	$C_{21}H_{20}O_9$	415.30	269	Flavonoids	0.87	[61]
10	Ferulic acid	7.09	$C_{10}H_{10}O_4$	193.05/195.05	149, 134	Phenolic acid	16.67	[66]
11	Quercetin-O-malonyl-hexoside	7.27	$C_{24}H_{22}O_{15}$	549.38	463	Flavonoids	2.69	[67]
12	Trihydroxy-9,14-octadecadienoic acid	8.71	$C_{18}H_{31}O_5$	327.27	291, 211, 183, 171, 99,	Fatty acid	2.73	[68]
13	Trihydroxyoctadecenoic acid	9.27	$C_{18}H_{34}O_5$	329.30	293, 229, 211, 171, 99	Fatty acid	0.70	[68]
14	Heptadecadienoic acid isomer	14.44	$C_{17}H_{30}O_2$	265.15	-	Fatty acid	0.71	[68]

observed at ν 1410 cm^{-1} suggests the existence of aromatic C = C bonds, while peaks at ν 1243 cm^{-1} and 1033 cm^{-1} correspond to the stretching vibrations of C–O–C bonds in alcohols. Asymmetric CH_2/CH_3 scissoring at ν 1416 cm^{-1} and COO– stretching at ν 1372 cm^{-1} were among the bands attributed to lipids [74, 75]. All stated peaks verified the existence of different phenolic and aromatic components in CPE (*i.e.*, flavonoids and phenolic acids).

The incorporation of CPE within the developed nanofibers was confirmed by absence of -OH stretching vibration of CPE. The spectrum pattern of CPE-loaded nanofibers also showed an increased intensity of the absorption vibrations band of C = O group at ν 1738 cm^{-1}.

XRD analysis of CPE-loaded-PMMA/Hal/CS/$CaCO_3$ nanofibers

Figure 5 illustrates XRD outlines of fabricated nanofibers. In Fig. 5A, pattern of pure CPE displayed a broad peak at 2θ ~ 22°, characteristic of its essentially amorphous structure, with a crystalline degree calculated at 56.45%. The XRD of Hal was recorded previously as two broader, less intense peaks at approximately 2θ values of 8.6° and 19° [76]. Notably, strong peak at 2θ ~ 13.4° is a characteristic peak of PMMA [77]. In Fig. 5B, a broad peak was observed between 2θ ~ 6°–25° along with a sharper peak near 2θ ~ 36°, suggesting an interaction between PMMA and Hal that contributes to the nanofiber amorphous nature. The crystallinity of E3 was 48.75%. In Fig. 5C, addition of CPE to PMMA/Hal combination (E5) resulted in further broadening, with a peak within the 2θ ~ 6°–23° range. E5 exhibited a crystallinity of 39.77%. Upon adding CS, a component with high crystallinity, to PMMA/Hal/CPE (E8), the resulting diffraction pattern (Fig. 5D) showed a broad peak centered at 2θ ~ 15°–25°, with the disappearance of characteristic CS peaks at 2θ ~ 19° and 23°. The crystallinity of E8 was 50.47%. This suggests strong interactions among PMMA, Hal, CPE, and CS. Pattern for E11, composed of PMMA, Hal, CPE, CS, and 1% $CaCO_3$ (Fig. 5E), display a shift in peak position from 2θ ~ 15°–25° to 2θ ~ 9°–23°, respectively with an increase in crystallinity, indicating effective

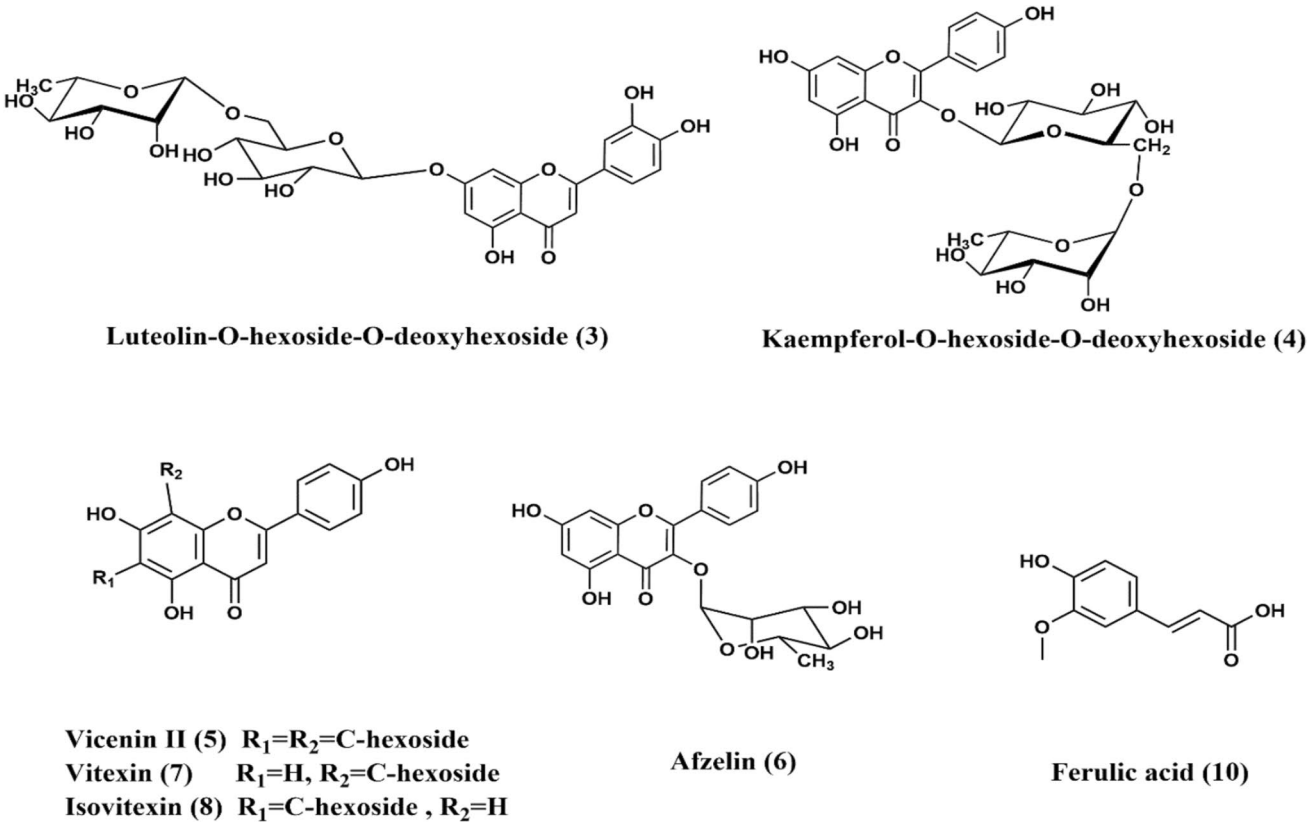

Fig. 2 Chemical structures of major compounds in methanol extract of *C. pepo* leaves which were identified by HPLC–MS/MS

integration and interaction of all components. The crystallinity for E11 was 35.89%. The pattern of E10, which incorporates 0.5% $CaCO_3$, is like E11, but with a slightly lower crystallinity (Fig. 5F), suggesting that $CaCO_3$ concentration influences the structural characteristics of the nanofibers. The crystallinity of E10 was 46.58%.

Swelling properties of nanofibers

Swelling behaviour of electrospun nanofiber scaffolds plays a crucial role in their effectiveness for wound healing applications, influencing their ability to absorb physiological fluids and support tissue regeneration. As shown in Fig. 6A, the swelling ratios of E3, E5, E8, E10, and E11 nanofibers were evaluated over 20 h, displaying varying behaviours when immersed in deionized water over time. E10, which includes PMMA, Hal, CS, $CaCO_3$, and CPE, demonstrated the highest swelling, reaching 998% after 20 h. This swelling is approaching due to the hydrophilic character of CS and the bioactive components in CPE, both of which promote water absorption. CS's ability to construct hydrogen bonds with water molecules enhances the swelling capacity. Conversely, E3, composed of PMMA and Hal, showed the lowest swelling, with a maximum of 119%. This can be attributed to the hydrophobic nature of PMMA. Consequently, the incorporation of CS and CPE enhances the swelling capacity of the nanofibers. E5 showed moderate swelling, reaching about 223%. These results highlight the influence of the nanofiber composition on swelling behaviour. Formulations incorporating hydrophilic materials, CS, and CPE, demonstrated higher swelling.

Hydrolytic degradation

Figure 6B represents the weight loss (%) over time for formulations E3, E5, E8, E10, and E11 immersed in phosphate buffer. The results show that the weight loss increases over time for all formulations. On day 1, E3 exhibited the lowest weight loss, while E10 and E11 showed the highest. By day 2, the weight loss for all formulations increased, with E10 still showing the most significant degradation. On day 3, E10 and E11 continued to show the highest weight loss, indicating that the presence of hydrophilic components, such as CPE and chitosan, accelerates degradation. These findings imply that the formulation composition plays a vital role in the degradation rate, with E10, which contains both CPE and $CaCO_3$, showing the highest weight loss, due to enhanced water absorption. The results confirm that the hydrophilic nature of the formulations

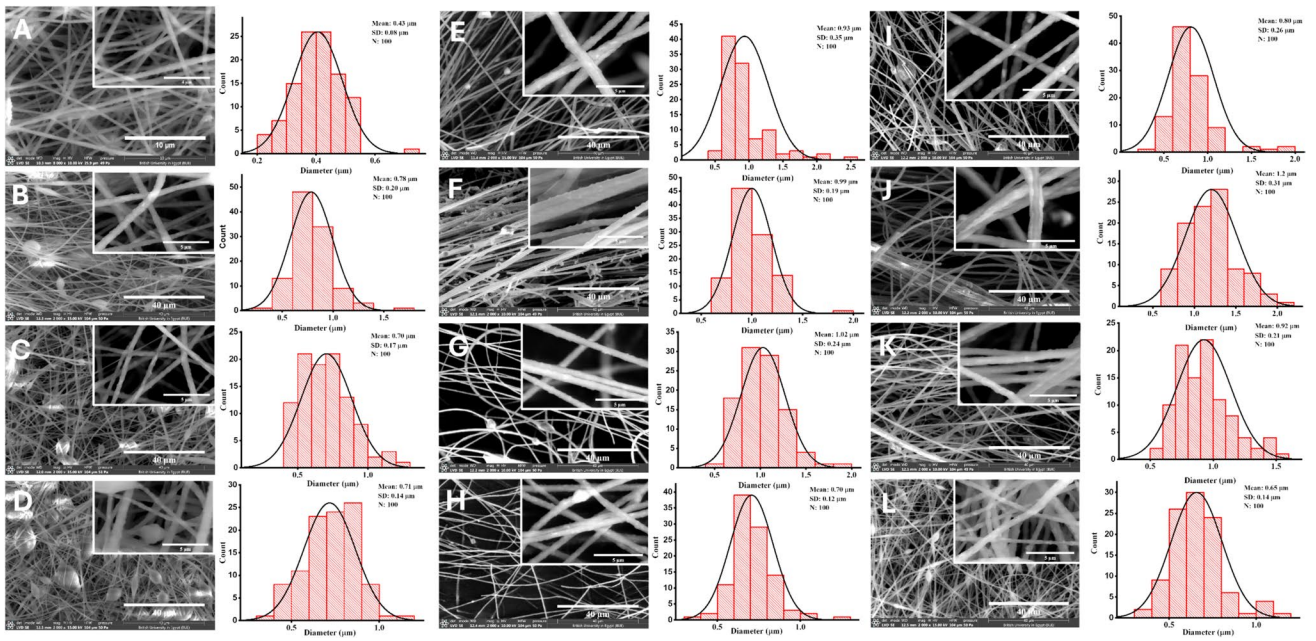

Fig. 3 SEM micrographs and diameter size distribution of the nanofibers at different magnifications, (**A**) PMMA, (**B**) E1, (**C**) E2, (**D**) E3, (**E**) E4, (**F**) E5, (**G**) E6, (**H**) E8, (**I**) E9, (**J**) E10, (**K**) E11, and (**L**) E12. The black line in the histograms shows *Gaussian* diameter size distributions

Table 3 EDX results for (**D**) E3, (**F**) E5, (**H**) E8, (**J**) E10

Scaffold	Element/Weight (%)		
	O K	AlK	SiK
E3	74.32	16.37	9.31
E5	45.82	29.84	24.34
E8	60.37	23.86	15.77
E10	64.53	27.83	7.64

affects the rate of degradation, with more hydrophilic formulations showing faster degradation.

In vitro antimicrobial studies

Agar-well diffusion method

Various antimicrobial nanomaterials and nanostructures have been developed to overcome antibiotic-resistant microbes [78]. The agar-well diffusion technique was employed to inspect the antimicrobial activities of the developed nanofibers. The inhibitory zone diameters of the tested scaffolds against multidrug-resistant human pathogens were measured [79]. The most significant inhibitory zone widths were found when tested versus Gram (+ Ve) bacteria rather than Gram (-Ve) bacteria and yeast (Fig. 7). Above the 95% scale, the modified confidence intervals are figured via the Tukey simultaneous examines. According to the tested formulation, each dot with whiskers represents the inhibitory effect distribution and shows the variance within the

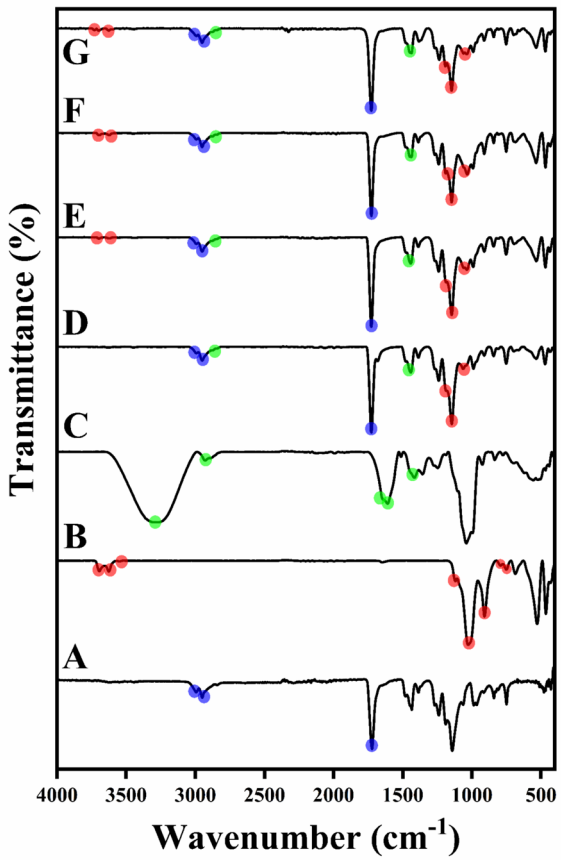

Fig. 4 FT-IR spectra of (**A**) PMMA, (**B**) Hal, (**C**) CPE, (**D**) E3, (**E**) E5, (**F**) E8, and (**G**) E10

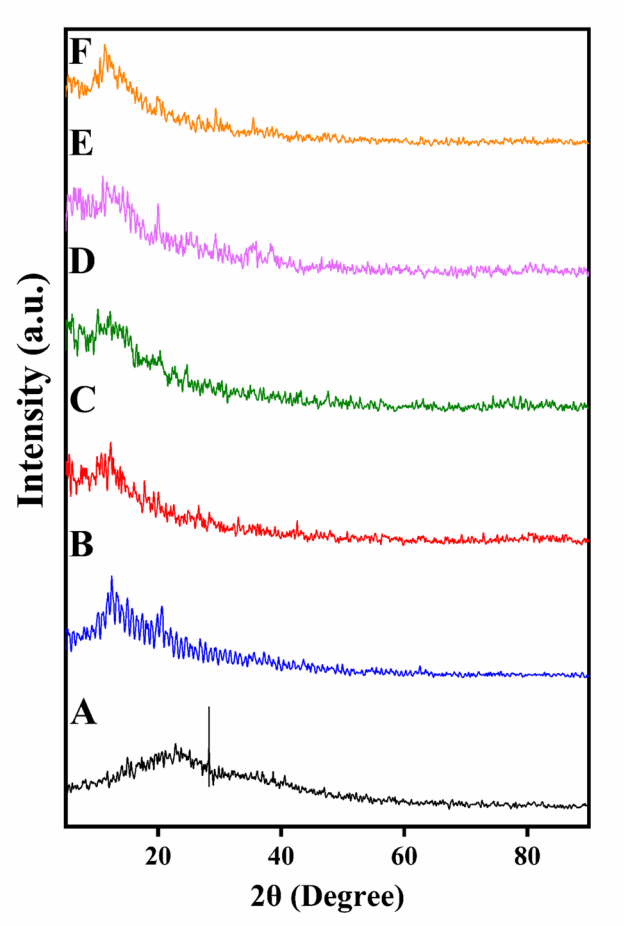

Fig. 5 XRD patterns of (**A**) CPE, (**B**) E3, (**C**) E5, (**D**) E8, (**E**) E10, and (**F**) E11

interquartile range. The box plot graph showed that all the information collected regarding the correlation between the examined formulations and antimicrobial activity was statistically grouped. According to the box-plot graph, E10 formulation exhibited the most potent antimicrobial properties. Additionally, there was a slight difference in the moderate antimicrobial action produced by E11 and E13 formulations (Fig. 7ii). According to *Tukey* simultaneous tests, the associated means are substantially different if an interval does not contain zero. As shown in (Fig. 7iii), only E11 with the E13 interval can cross through the zero line. E10 formulation does not contain zero; hence, it differs statistically from the other formulations under investigation. As can be seen from Table S1 (Supplementary materials), E3 displayed no antimicrobial activity (*i.e.*, no distinct inhibitory zones) against the studied human pathogens. Furthermore, E8 formulation demonstrated the lowest inhibitory zone widths against all tested pathogens. The differences among all tested formulations that do not have the same superscript letter are statistically significant. As shown in (Fig. 7iii), E10 formulation notably produced the highest inhibitory values against all tested human pathogens, especially *Gram-positive* bacteria. As shown in (Table S1, Supplementary materials), E10 formulation treatment resulted in the highest inhibitory zone widths against *Bacillus cereus* (22.31 ± 2.55 mm), *Staphylococcus aureus* (21.05 ± 1.09 mm), and *Staphylococcus epidermidis* (20.31 ± 0.21 mm). Among the tested *Gram-negative* bacteria and yeast cells, *Escherichia coli* and *Candida glabrata* treated with E10 displayed the highest inhibitory zones (18.04 ± 1.21 and 19.09 ± 0.66 mm, respectively).

A spectrophotometric antibiofilm assay was utilized to assess further the in vitro antimicrobial activity of the tested formulations, utilizing biofilm reduction percentages (Table S2, Supplementary materials). E10 formulation demonstrated superior antimicrobial activity against all tested pathogens, as depicted in Fig. 8i, compared to E8 and E11 formulations, which exhibited moderate antimicrobial effects. In contrast, E3 showed minimal biofilm inhibition against all tested pathogens. Statistical analysis, including *ANOVA* and *Tukey's post-hoc* test, was developed to evaluate the significance of the observed antibiofilm activity. The data were further organized using statistical clustering to explore the relationship between the formulations and their antimicrobial activity. Box plots and interval graphs illustrated the distributions of inhibitory effects corresponding to each formulation. Notably, E10 exhibited the highest antibiofilm activity (Fig. 8ii), with *Tukey–Kramer post-hoc* analysis confirming statistically significant differences in efficacy (Fig. 8iii). The mean values for E10 did not include the zero line in the confidence intervals, indicating its superior efficacy. According to Table S2 (Supplementary materials), the highest percentages of biofilm reduction were observed in Bacillus subtilis ($96.55 \pm 0.87\%$), *Bacillus cereus* ($95.09 \pm 1.11\%$), and *Staphylococcus aureus* ($92.05 \pm 0.98\%$) treated with E10. *Escherichia coli* ($79.29 \pm 2.25\%$) and *Candida albicans* ($73.02 \pm 2.33\%$) also showed substantial, albeit lower, biofilm inhibition. These results emphasize the potent antimicrobial and antibiofilm properties of E10, highlighting its potential for broader applications in pathogen control.

To gain further insights into time-kill kinetics of E10, the most effective antimicrobial tested formulation, a time-kill study was performed against the most sensitive pathogens (*i.e.*, *Bacillus subtilis* (*Gram-positive* bacteria), *Escherichia coli* (*Gram-negative* bacteria), and *Candida albicans* (yeast cells)). The selected pathogens were treated with E10 and the $\log_{10}$ CFU/mL was measured compared to the untreated corresponding cells (Fig. 9i). The pathogens treated with E10 and their quantitative $\log_{10}$ CFU/mL reduction are listed in Table S3 (Supplementary materials). After 24 h, the tested formulation (E10) effectively decreased the planktonic viable counts of all tested pathogens (Fig. 9ii). After 48 h, *Bacillus subtilis* ($99.73 \pm 0.51\%$) treated with E10 demonstrated the highest percentage of biofilm reduction, followed

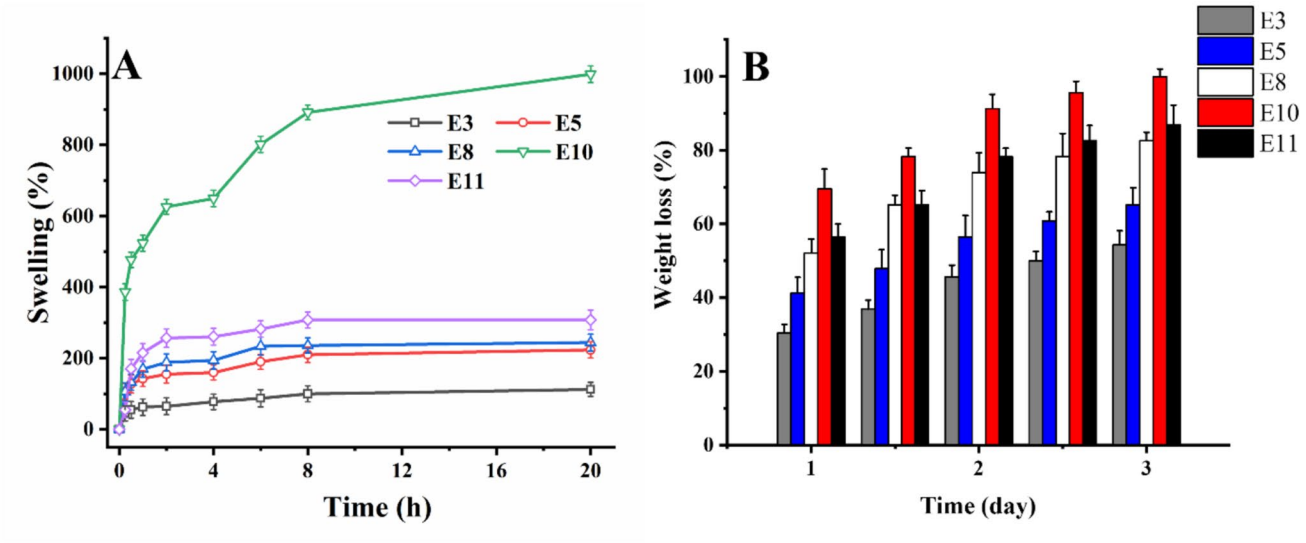

Fig. 6 **(A)** Swelling of electrospun nanofibers was evaluated at different time intervals between 0 and 20 h. **(B)** Hydrolytic degradation of electrospun nanofibers immersed in PBS for 3 days

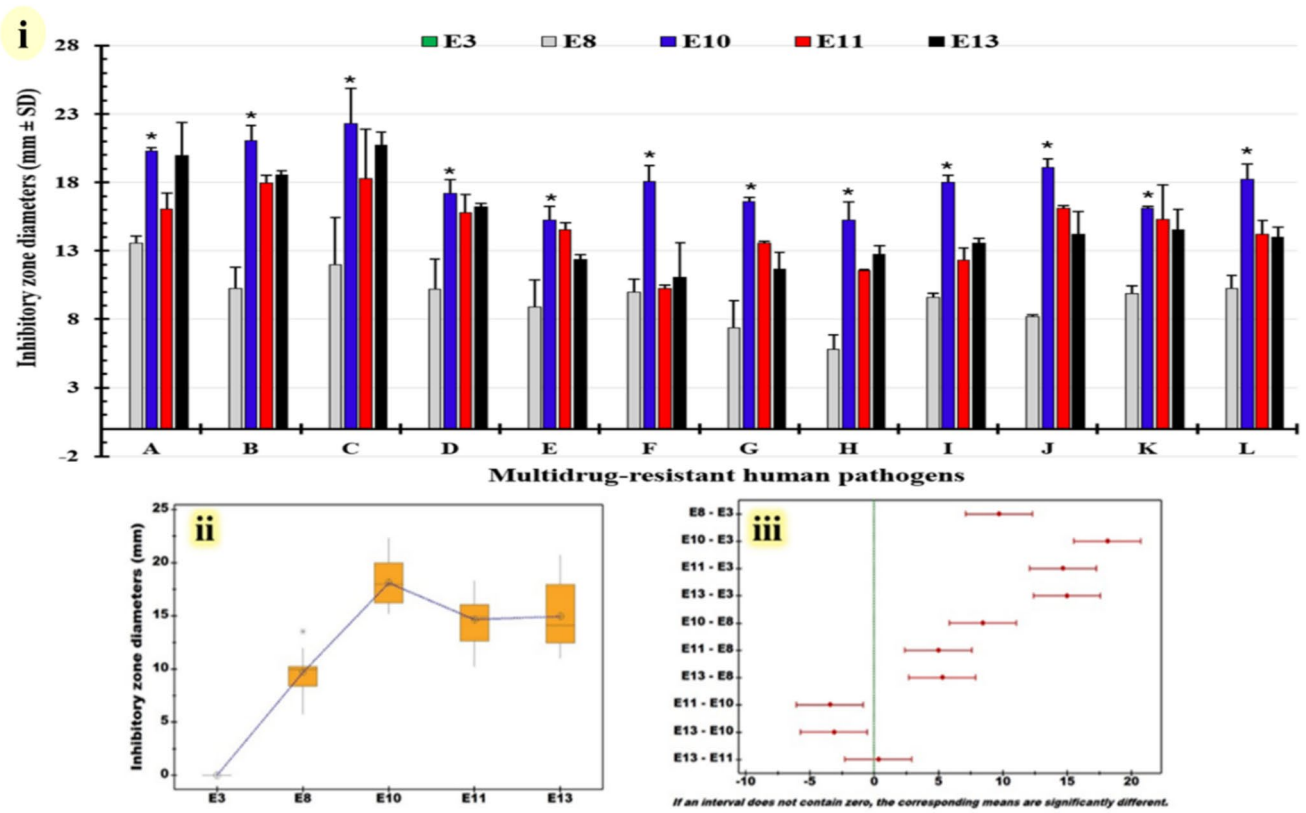

Fig. 7 Agar-well diffusion test for the tested formulations (E3, E8, E10, E11, and E13) against **A:** *Staphylococcus epidermidis*, **B:** *Staphylococcus aureus*, **C:** *Bacillus cereus*, **D:** *Bacillus subtilis,* **E:** *Salmonella paratyphi*, **F:** *Escherichia coli*, **G:** *Klebsiella pneumoniae*, **H:** *Pseudomonas aeruginosa* **I:** *Candida krusei*, **J:** *Candida glabrata*, **K:** *Candida albicans*, and **L:** *Candida parapsilosis.* (**i**) The charts for the calculated inhibition zones, (**ii**) the interval graph shows the inhibitory rate distributions equivalent to the examined formulations via box-plot graph, and (**iii**) simultaneous Tukey outcomes for examining the overall groups alteration. *Represents the biggest inhibitory zone

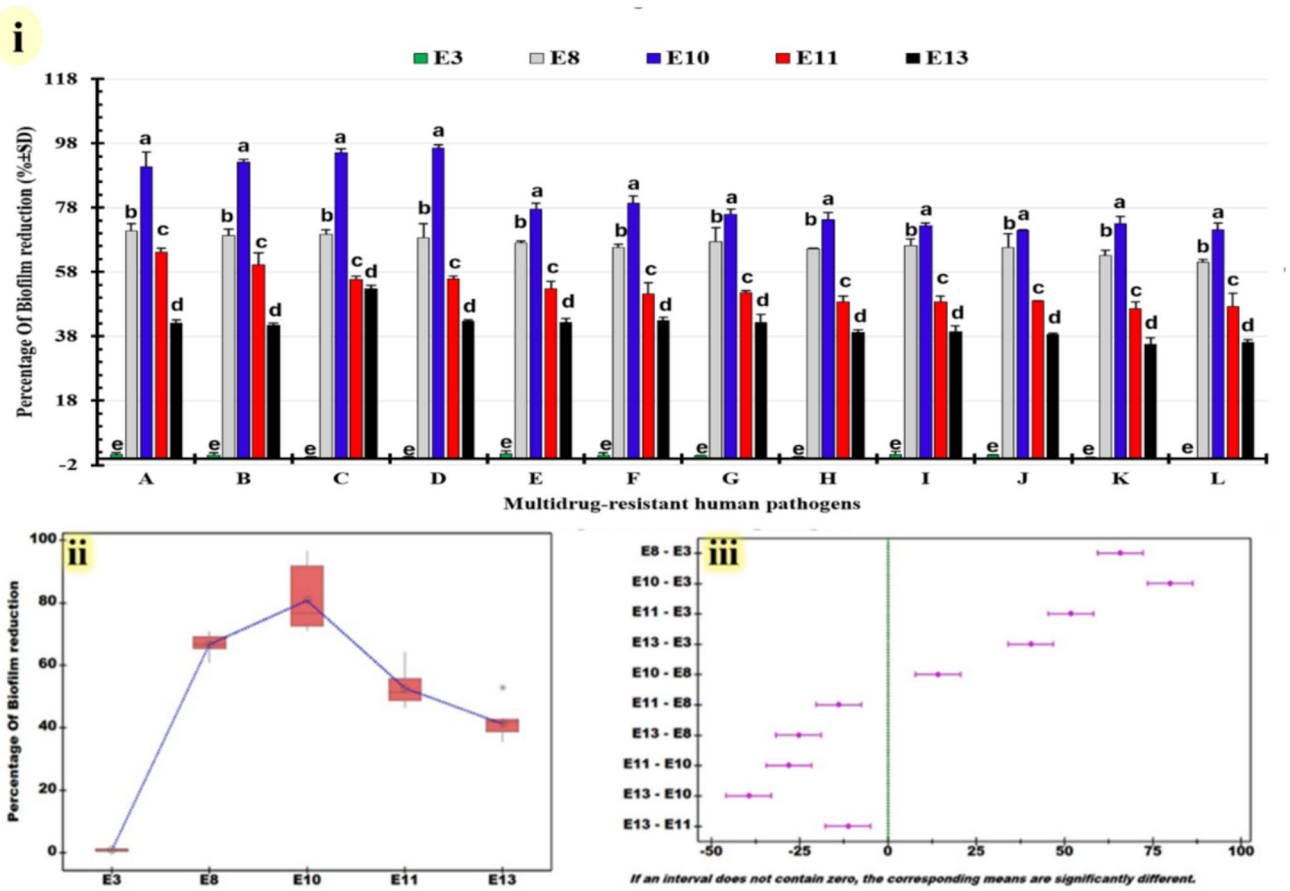

Fig. 8 Spectrophotometric antibiofilm assay against **A:** *Salmonella paratyphi*, **B:** *Escherichia coli*, **C:** *Klebsiella pneumoniae*, **D:** *Pseudomonas aeruginosa*, **E:** *Staphylococcus epidermidis*, **F:** *Staphylococcus aureus*, **G:** *Bacillus cereus*, **H:** *Bacillus subtilis*, **I:** *Candida krusei*, **J:** *Candida glabrata*, **K:** *Candida albicans*, and **L:** *Candida parapsilosis* treated with E3, E8, E10, E11, and E13 (CPE). (**i**) The diagram displays the percentage of biofilm drop, (**ii**) the box-plot graph displays biofilm drop value distributions equivalent to the tested formulations via *Tukey–Kramer post-hoc* analysis, (**iii**) and simultaneous *Tukey* outcomes for analyzing the overall group's difference. * Differences in the superscript letters are statistically significant at $p \leq 0.05$

by *Candida albicans* (98.01 ± 1.98%) and *Escherichia coli* (93.76 ± 0.21%) treated with the same formulation.

In vivo assessment

Wound healing rate analysis

This study utilized a wound healing model to evaluate the healing capacity of the fabricated nanofibers. Representative images of wounds at various time points are demonstrated in Fig. 10. Wound contraction usually occurs between the first and second weeks after injury [80]. The effectiveness of scaffolds in enhancing wound contraction is represented by the percentage of wound closure over time (Fig. 11). Wound healing progression was systematically recorded at specific intervals (0, 3, 7, 10, and 14 d), as depicted in Fig. 10. After 7 days, wound closure in the control group was 46.6 ± 0.3%, while wound closure in groups II, III, and IV treated with E3 (PMMA/Hal), E12 (PMMA/Hal/CS/$CaCO_3$) and E10 (PMMA/Hal/CPE/CS/$CaCO_3$) increased to 61.2 ± 0.1%, 78.1 ± 0.1% and 83.7 ± 0.03%, respectively (Fig. 11). After 14 days, wound closure in the control group was 76.8 ± 0.05%, while wound closure in groups II, III, and IV increased to 92.03 ± 0.04%, 96.8 ± 0.1%, and 99.9 ± 0.001%, respectively (Fig. 11). The enhanced wound healing demonstrated in group II, as compared to the untreated group I, might be attributed to the presence of Hal in the nanofiber. The further acceleration of wound healing observed in group III might be attributed to incorporation of CS and $CaCO_3$. Group IV, treated with E10 that incorporated CPE, CS, and $CaCO_3$, demonstrated a noteworthy drop in wound size at all studied time intervals as compared to group III, which was treated with extract-free nanofiber (E12), providing evidence for the wound healing capacity of the CPE.

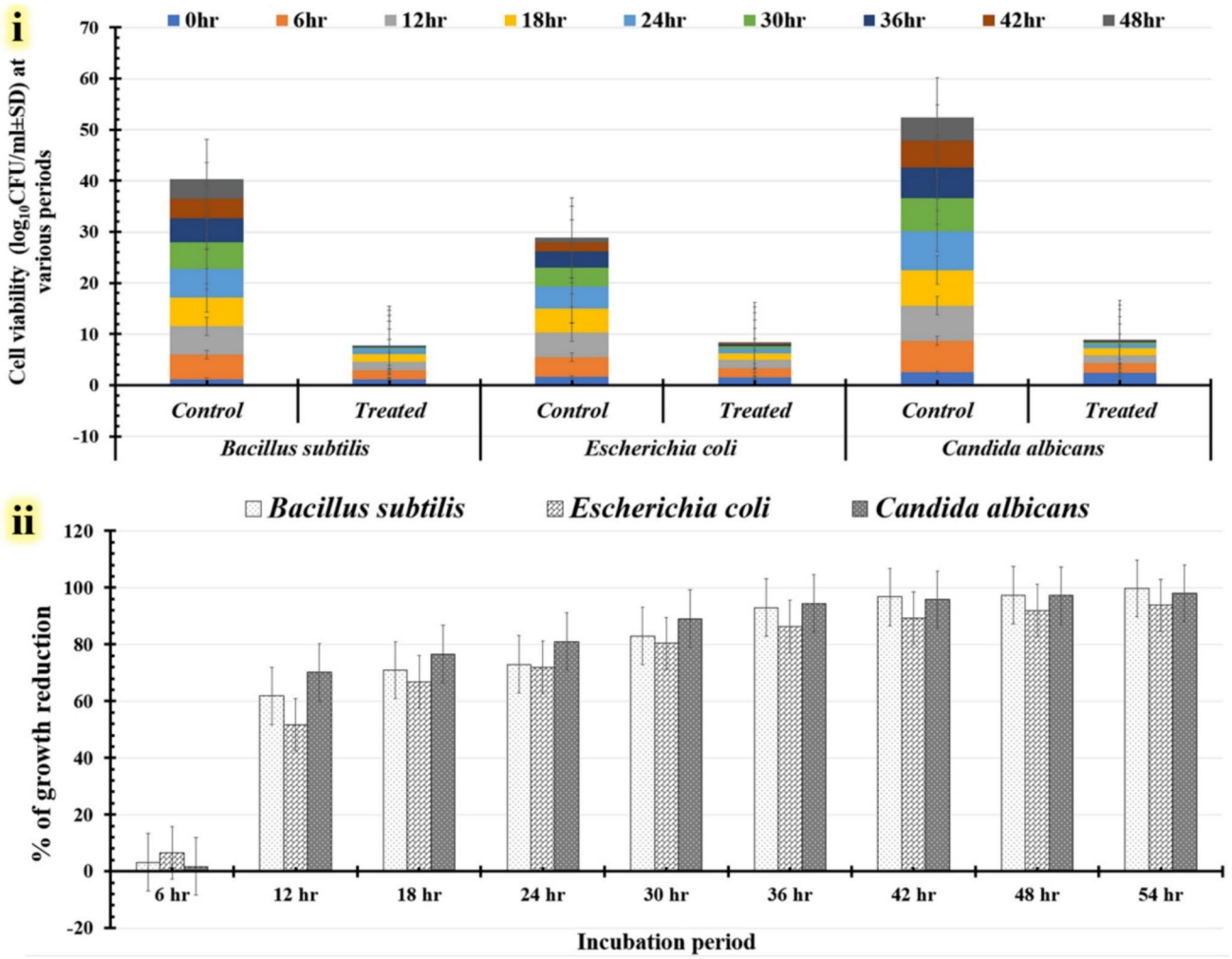

Fig. 9 (**i**) Cell viability of multidrug-resistant human pathogens treated with E10 compared to untreated throughout the incubation period, (**ii**) Percentage of growth reduction chart

Histopathological analysis

Histopathological results were concordant with the in vivo wound closure assay as revealed in Fig. 12. The untreated control group exhibited realize epithelial ulceration, screened by a fibrinopurulent exudate, with underlying granulation tissue, neovascularization, and non-identifiable collagen bundles. In group II, there is mild evidence of wound healing in partial epithelialization with attenuated epithelium and minimal replacement of the underlying granulation tissue via creeping collagen fibers at the sides of the wound. Groups III and IV showed marked improvement in the healing process in the form of epithelial closure and replacement of granulation tissue by collagen fibers, with minimal residual granulation tissue in group IV.

Conclusions

In conclusion, the electrospun PMMA/Hal/CS/$CaCO_3$ nanofibers loaded with CPE was successfully fabricated for wound healing applications. The optimal formulation (E10), consisting of 30% PMMA, 5% Hal, 1% CPE, 1% CS, and 0.5% $CaCO_3$, was characterized using SEM, FTIR, and XRD. SEM images showed smooth, uniform nanofibers with good CPE dispersion, while FTIR and XRD

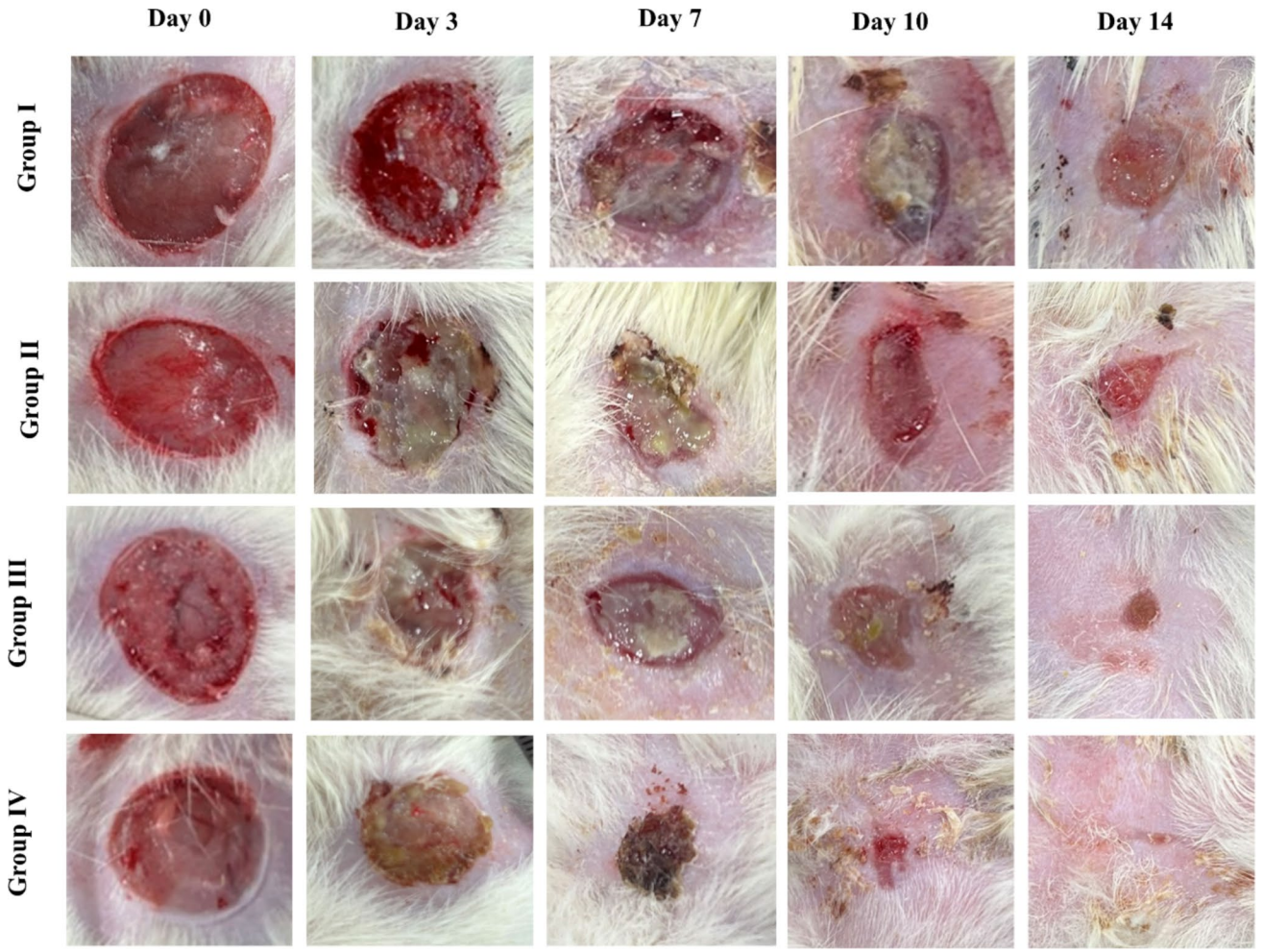

Fig. 10 Representative photographic images of wounds for Group I (sterile gauze), Group II (treated with E3), Group III (treated with E12), and Group IV (treated with E10) on days 0, 3, 7, 10, and 14

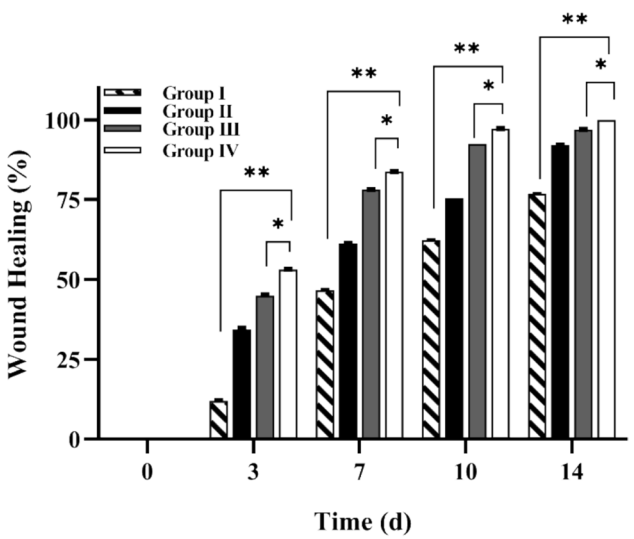

Fig. 11 Wound closure percentages on days 3, 7, 10, and 14 in the untreated (control) and the treated groups. *Statistical significance among Group IV and Group III ($p < 0.0001$), **Statistical significance among Group IV and Group I ($p < 0.0001$)

analyses confirmed the successful integration of CPE into the nanofiber matrix. The antimicrobial activity of the E10 formulation was evaluated using the agar well diffusion method, demonstrating strong efficacy against Gram-positive bacteria, including *Staphylococcus aureus* (22.31 mm) and *Bacillus cereus* (21.05 mm), as well as significant activity against *Escherichia coli*. In vivo studies indicated that E10 significantly accelerated wound closure, achieving 99.9% healing by day 14. Histological analysis revealed increased macrophage infiltration, neovascularization, and fibroblast proliferation by day 7, with significant collagen deposition and epithelial regeneration by day 14.

This study highlights that CPE-loaded electrospun nanofibers possess potent antimicrobial properties and significantly enhance wound healing, making them a promising candidate for advanced wound healing applications and potential clinical use.

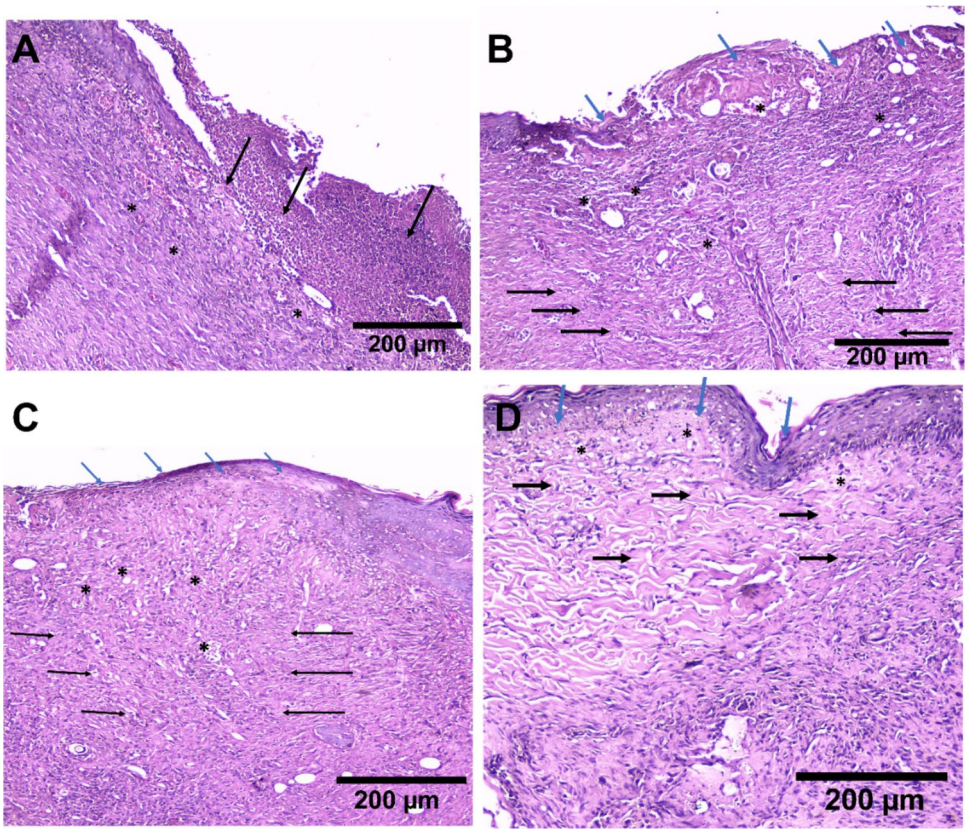

Fig. 12 Histopathology of wounds in control and nanofibers-treated skin wounds stained by H&E stain. (**A**) Photomicrograph of skin wound (**Group I**) showing epithelial ulceration screened by fibrinopurulent exudate (black arrows) through underlying granulation tissue and neovascularization (*). Non evidence of collagen formation. (**B**) Photomicrograph of skin wound (**Group II**) showing partial epithelialization with attenuated epithelium (blue arrows). There is minimal replacement of the underlying granulation tissue (*) via creeping collagen fibers at the sides of the wound (black arrows). (**C**) Photomicrograph of skin wound (**Group III**) showing complete epithelialization with attenuated epithelium (blue arrows) with no residual ulceration. There is minimal residual granulation tissue (*) replaced by creeping collagen fibers at the sides and base of the wound (black arrows), indicating better healing in **Group III** than in **Group II**. (**D**) Photomicrograph of skin wound (**Group IV**) showing complete epithelialization with standard epithelial thickness (blue arrows) and no residual ulceration. The granulation tissue (*) shows near total replacement by collagen fibers in the figure (black arrows), indicating better healing in Group IV than in Groups II & III

Supplementary Information The online version contains supplementary material available at https://doi.org/10.1007/s13346-026-02124-7.

Author Contributions Author Contributions: Esraa B. Abdelazim: Methodology, formal analysis, investigation, data curation, writing – original draft. Shaza H. Aly: Methodology, investigation, writing – original draft. Shahira H. EL-Moslamy: Methodology and discussion of antimicrobial sections. Hend H. Mohamed: Methodology, investigation. Enas A. Abdul-Baki: Methodology, investigation. Marwa Mosaad Shakweer: Methodology, investigation, writing – original draft. Noura G. Eissa: Formal analysis, writing – reviewing & editing. Elbadawy A. Kamoun: Methodology, supervision, resources, writing – reviewing & editing the final draft. Mahmoud Elsabahy: Conceptualization, methodology, supervision, writing – reviewing & editing. Samar A Salim: Conceptualization, formal analysis, methodology, supervision, writing – reviewing & editing original draft. All authors have read and agreed to the published version of the manuscript.

Funding Open access funding provided by The Science, Technology & Innovation Funding Authority (STDF) in cooperation with The Egyptian Knowledge Bank (EKB).

Data Availability No datasets were generated or analysed during the current study.

Declarations

Ethics approval and consent to participate A protocol has been conducted is the Animal Care and Use the institutional ethical Committee of Faculty of Pharmacy, Badr University in Cairo (BUC), Egypt (*BUC-IACUC-240623–98*) and the rules of the National Research Council's guide for the care and use of laboratory animals. Furthermore, animal experiments followed the arrive guidelines and UK Animals (Scientific Procedures) Act, 1986, and associated guidelines, EU Directive 2010/63/EU for animal experiments.

Competing interests The authors declare no competing interests.

Open Access This article is licensed under a Creative Commons Attribution 4.0 International License, which permits use, sharing, adaptation, distribution and reproduction in any medium or format, as long as you give appropriate credit to the original author(s) and the source,

provide a link to the Creative Commons licence, and indicate if changes were made. The images or other third party material in this article are included in the article's Creative Commons licence, unless indicated otherwise in a credit line to the material. If material is not included in the article's Creative Commons licence and your intended use is not permitted by statutory regulation or exceeds the permitted use, you will need to obtain permission directly from the copyright holder. To view a copy of this licence, visit http://creativecommons.org/licenses/by/4.0/.

References

1. Okur ME, Karadağ AE, Okur NÜ, Özhan Y, Sipahi H, Ayla Ş, et al. In vivo wound healing and in vitro anti-inflammatory activity evaluation of *Phlomis russeliana* extract gel formulations. Molecules. 2020;25:1–17. https://doi.org/10.3390/molecules25112695.
2. Bakr RO, Amer RI, Attia D, Abdelhafez MM, Al-Mokaddem AK, El Gendy AN, et al. In-vivo wound healing activity of a novel composite sponge loaded with mucilage and lipoidal matter of *Hibiscus* species. Biomed Pharmacother. 2021;135:111225. https://doi.org/10.1016/j.biopha.2021.111225.
3. Imran M, Sharma JN, Kamal M, Asif M. Standardization and wound-healing activity of petroleum, ethanolic and aqueous extracts of *Ficus benghalensis* leaves. Pharm Chem J. 2021;54:1057–62. https://doi.org/10.1007/s11094-021-02319-x.
4. Elsabahy M, Heo GS, Lim SM, Sun G, Wooley KL. Polymeric nanostructures for imaging and therapy. Chem Rev. 2015;115:10967–1011. https://doi.org/10.1021/acs.chemrev.5b00135.
5. Yao CH, Chen KY, Chen YS, Li SJ, Huang CH. *Lithospermi radix* extract-containing bilayer nanofiber scaffold for promoting wound healing in a rat model. Mater Sci Eng C Mater Biol. 2019;96:850–8. https://doi.org/10.1016/j.msec.2018.11.053.
6. Samarajeewa S, Ibricevic A, Gunsten SP, Shrestha R, Elsabahy M, Brody SL, et al. Degradable cationic shell cross-linked knedel-like nanoparticles: synthesis, degradation, nucleic acid binding, and in vitro evaluation. Biomacromol. 2013;14:1018–27. https://doi.org/10.1021/bm3018774.
7. Zhang F, Khan S, Li R, Smolen JA, Zhang S, Zhu G, et al. Design and development of multifunctional polyphosphoester-based nanoparticles for ultrahigh paclitaxel dual loading. Nanoscale. 2017;9:15773–7. https://doi.org/10.1039/c7nr05935c.
8. Irani M, Abadi PGS, Ahmadian-Attari MM, Rezaee A, Kordbacheh H, Goleij P. In vitro and in vivo studies of Dragon's blood plant (*D. cinnabari*)-loaded electrospun chitosan/PCL nanofibers: Cytotoxicity, antibacterial, and wound healing activities. Int J Biol Macromol. 2024;257:128634. https://doi.org/10.1016/j.ijbiomac.2023.128634.
9. Eissa NG, Elsabahy M. Applying drug-loaded electrospun nanofibers to antimicrobial-resistant skin infections. Nanomedicine. 2025;20:2601–4. https://doi.org/10.1080/17435889.2025.2528592.
10. Shahriar SMS, Mondal J, Hasan MN, Revuri V, Lee DY, Lee YK. Electrospinning nanofibers for therapeutics delivery. Nanomaterials. 2019. https://doi.org/10.3390/nano9040532.
11. Fathi HA, Abdelkader A, AbdelKarim MS, Abdelaziz AA, El Mokhtar MA, Allam A, et al. Electrospun vancomycin-loaded nanofibers for management of methicillin-resistant *Staphylococcus aureus*-induced skin infections. Int J Pharm. 2020;586:119620. https://doi.org/10.1016/j.ijpharm.2020.119620.
12. Zhang Y, Zhang C, Wang Y. Recent progress in cellulose-based electrospun nanofibers as multifunctional materials. Nanoscale Adv. 2021;3:6040–7. https://doi.org/10.1039/d1na00508a.
13. Elbadry AMM, Kamoun EA, Elsabahy M, Helmy MS, kh M, EL-Moslamy SH, et al. Enhancing topical delivery of N-acetylcysteine and collagen via a novel electrospun collagen/PMMA nanofibrous mats as facial mask development: nanofibers optimization and in vitro experiments. J Drug Deliv Sci Technol. 2025;104:106566. https://doi.org/10.1016/j.jddst.2024.106566.
14. Liu X, Xu H, Zhang M, Yu DG. Electrospun medicated nanofibers for wound healing: review. Membranes (Basel). 2021. https://doi.org/10.3390/membranes11100770.
15. Kamoun EA, Elsabahy M, Elbadry AMM, Abdelazim EB, Mohsen AA, Aleem MA, et al. Recent progress of polymer-based biosensors for cancer diagnostic applications: natural versus synthetic polymers. ACS Omega. 2025. https://doi.org/10.1021/acsomega.4c10652.
16. Goher SS, Abdelazim EB, Aleem MA, Salim SA. Development and characterization of PMMA/PVP nanofiber-loaded bioactive agents with enhanced breast cancer activity. Arab J Sci Eng. 2025. https://doi.org/10.1007/s13369-025-10288-6.
17. Salim SA, Ali MAM, Abed T, Chaudhary AA, Boufahja F, Hasanein AM, et al. Coumarin/nitrogen-bearing heterocyclic hybrid-loaded electrospun PMMA/PVP nanofibrous scaffolds for accelerating topical wound healing rates: synthesis and in vitro bio-evaluation. RSC Adv. 2025;15:36731–48. https://doi.org/10.1039/d5ra02535d.
18. Ura DP, Karbowniczek JE, Szewczyk PK, Metwally S, Kopyściański M, Stachewicz U. Cell integration with electrospun PMMA nanofibers, microfibers, ribbons, and films: a microscopy study. Bioengineering. 2019;6:1–12. https://doi.org/10.3390/bioengineering6020041.
19. Ashraf H, Salim SA, EL-Moslamy SH, Loutfy SA, Kamoun EA. An injectable in situ forming collagen/alginate/CaSO4 composite hydrogel for tissue engineering applications: optimization, characterization and in vitro assessments. Arab J Sci Eng. 2024. https://doi.org/10.1007/s13369-024-08922-w.
20. Mascarenhas-Melo F, Peixoto D, Aleixo C, Maria MB, Raza F, Pawar KD, et al. Nanoclays for wound management applications. Drug Deliv Transl Res. 2023;13:924–45. https://doi.org/10.1007/s13346-022-01279-3.
21. Salim SA, Taha AA, Khozemy EE, EL-Moslamy SH, Kamoun EA. Electrospun zinc-based metal organic framework loaded-PVA/chitosan/hyaluronic acid interfaces in antimicrobial composite nanofibers scaffold for bone regeneration applications. J Drug Deliv Sci Technol. 2022;76:103823. https://doi.org/10.1016/j.jddst.2022.103823.
22. Nageeb El-Helaly S, Abd-Elrasheed E, Salim SA, Fahmy RH, Salah S, El-Ashmoony MM. Green nanotechnology in the formulation of a novel solid dispersed multilayered core-sheath raloxifene-loaded nanofibrous buccal film; in vitro and in vivo characterization. Pharmaceutics. 2021;13:474.
23. Salim SA, Loutfy SA, El-Fakharany EM, Taha TH, Hussien Y, Kamoun EA. Influence of chitosan and hydroxyapatite incorporation on properties of electrospun PVA/HA nanofibrous mats for bone tissue regeneration: nanofibers optimization and in-vitro assessment. J Drug Deliv Sci Technol. 2021;62:102417.
24. Ibrahim RM, Kamoun EA, Badawi NM, EL-Moslamy SH, kh M, Salim SA. Cutting-edge biomaterials for advanced biomedical uses: self-gelation of l-arginine-loaded chitosan/PVA/vanillin hydrogel for accelerating topical wound healing and skin regeneration. RSC Adv. 2024;14:31126–42. https://doi.org/10.1039/D4RA04430D.
25. Karamat-Iradmousa M, Karimi H, Mahboubi A, Rabbani S, Kamalinejad M, Haeri A. Bi-layered nanofibers loaded with pomegranate flowers extract as a novel wound dressing: fabrication, characterization, and in vivo healing promotion. Ind Crops Prod. 2023;202:117042. https://doi.org/10.1016/j.indcrop.2023.117042.

26. Subramaniam T, Fauzi MB, Lokanathan Y, Law JX. The role of calcium in wound healing. Int J Mol Sci. 2021. https://doi.org/10.3390/ijms22126486.
27. Abed T, Aly SH, Salim SA, Haikal RR, Shams-Eldin R, EL-Moslamy SH, et al. Optimizing hydrogel performance composed of Japanese pagoda tree extract loaded-gelatin-sodium alginate-polyethylene oxide for biomedical applications: influence incorporated calcium-based metal organic frameworks and zinc oxide NPs. Int J Biol Macromol. 2025;310:143526. https://doi.org/10.1016/j.ijbiomac.2025.143526.
28. Abed T, Aly SH, Salim SA, EL-Moslamy SH, Abdelazim EB, Helmy MS, et al. Evaluation of an in situ forming composite hydrogel based on gelatin–sodium alginate–polyethylene oxide for biomedical applications: effect of incorporated *Sophora japonica* on hydrogel performance. New J Chem. 2025;49:19226–39. https://doi.org/10.1039/D5NJ02739J.
29. Salim SA, Abed T, Abdelazim EB, Eissa NG, Elsabahy M, Kamoun EA. Exploring the therapeutic potential of plant extract-loaded polymeric nanoparticles for advanced wound healing: a comprehensive review. Arab J Sci Eng. 2025;50:14351–69.
30. Abdelazim EB, Abed T, Goher SS, Alya SH, El-Nashar HAS, EL-Moslamy SH, et al. In vitro and in vivo studies of *Syzygium cumini*-loaded electrospun PLGA/PMMA/collagen nanofibers for accelerating topical wound healing. RSC Adv. 2024;14:101–17. https://doi.org/10.1039/d3ra06355k.
31. Mirzaei E, Sarkar S, Rezayat SM, Faridi-Majidi R. Herbal extract loaded chitosan-based nanofibers as a potential wound-dressing. J Adv Med Sci Appl Technol. 2016;2:141. https://doi.org/10.18869/nrip.jamsat.2.1.141.
32. Amer AA, Mohammed RS, Hussein Y, Ali ASM, Khalil AA. Development of *Lepidium sativum* extracts/PVA electrospun nanofibers as wound healing dressing. ACS Omega. 2022;7:20683–95. https://doi.org/10.1021/acsomega.2c00912.
33. Ndlovu SP, Motaung KSCM, Adeyemi SA, Ubanako P, Ngema L, Fonkui TY, et al. Sodium alginate-based nanofibers loaded with *Capparis Sepiaria* plant extract for wound healing. J Biomater Sci Polym Ed. 2024;35:2380–401. https://doi.org/10.1080/09205063.2024.2381375.
34. Fayemi OE, Ekennia AC, Katata-Seru L, Ebokaiwe AP, Ijomone OM, Onwudiwe DC, et al. Antimicrobial and wound healing properties of polyacrylonitrile-Moringa extract nanofibers. ACS Omega. 2018;3:4791–7. https://doi.org/10.1021/acsomega.7b01981.
35. Aly SH, El-Hassab MA, Elhady SS, Gad HA. Comparative metabolic study of *Tamarindus indica* L.'s various organs based on GC/MS analysis, in silico and in vitro anti-inflammatory and wound healing activities. Plants. 2022;12:87. https://doi.org/10.3390/plants12010087.
36. Aly SH, Elissawy AM, Mahmoud AMA, El-Tokhy FS, Mageed SSA, Almahli H, et al. Synergistic effect of *Sophora japonica* and *Glycyrrhiza glabra* flavonoid-rich fractions on wound healing: in vivo and molecular docking studies. Molecules. 2023;28:2994.
37. Caili FU, Huan S, Quanhong LI. A review on pharmacological activities and utilization technologies of pumpkin. Plant Foods Hum Nutr. 2006;61:70–7.
38. Adnan M, Gul S, Batool S, Fatima B, Rehman A, Yaqoob S, et al. A review on the ethnobotany, phytochemistry, pharmacology and nutritional composition of *Cucurbita pepo* L. J Phytopharmacol. 2017;6:133–9.
39. Asowata-Ayodele AM, Afolayan AJ, Otunola GA. Ethnobotanical survey of culinary herbs and spices used in the traditional medicinal system of Nkonkobe Municipality, Eastern Cape, South Africa. S Afr J Bot. 2016;104:69–75.
40. Akubugwo EI, Emmanuel O, Ekweogu CN, Ugbogu OC, Onuorah TR, Egeduzu OG, et al. GC-MS analysis of the phytochemical constituents, safety assessment, wound healing and anti-inflammatory activities of *cucurbita pepo* leaf extract in rats. Sci Pharm. 2022;90:64.
41. Ayoub IM, Korinek M, El-Shazly M, Wetterauer B, El-Beshbishy HA, Hwang TL, et al. Anti-allergic, anti-inflammatory and anti-hyperglycemic activity of *chasmanthe aethiopica* leaf extract and its profiling using lc/ms and glc/ms. Plants. 2021. https://doi.org/10.3390/plants10061118.
42. Aly SH, Elissawy AM, Salah D, Alfuhaid NA, Zyaan OH, Mohamed HI, et al. Phytochemical investigation of three *Cystoseira* species and their larvicidal activity supported with in silico studies. Mar Drugs. 2023;21:1–17. https://doi.org/10.3390/md21020117.
43. Aly SH, Elissawy AM, Mahmoud AMA, El-tokhy FS, Mageed SSA, Almahli H, et al. Synergistic effect of *Sophora japonica* and *Glycyrrhiza glabra* flavonoid-rich fractions on wound healing : in vivo and molecular docking studies. Molecules. 2023;28:2994. https://doi.org/10.3390/molecules28072994.
44. Khosravi N, Zarabi M, Dehghan MM, Farzad-Mohajeri S, Amini-anfar H, Shafie M, et al. Bioinspired wound dressing: investigating coelomic fluid-enhanced chitosan/polyvinyl alcohol nanofibers. Int J Pharm. 2024;666:124765. https://doi.org/10.1016/j.ijpharm.2024.124765.
45. Salim SA, Kamoun EA, Evans S, Taha TH, El-Fakharany EM, Elmazar MM, et al. Novel oxygen-generation from electrospun nanofibrous scaffolds with anticancer properties: synthesis of PMMA-conjugate PVP-H2O2nanofibers, characterization, and: in vitro bio-evaluation tests. RSC Adv. 2021;11:19978–91. https://doi.org/10.1039/d1ra02575a.
46. Doğan D, Karaduman FR, Horzum N, Metin AÜ. Boron nitride decorated poly(vinyl alcohol)/poly(acrylic acid) composite nanofibers: a promising material for biomedical applications. J Mech Behav Biomed Mater. 2023;141:105773. https://doi.org/10.1016/j.jmbbm.2023.105773.
47. Hayat S, Ashraf A, Zubair M, Aslam B, Siddique MH, Khurshid M, et al. Biofabrication of ZnO nanoparticles using *Acacia arabica* leaf extract and their antibiofilm and antioxidant potential against foodborne pathogens. PLoS ONE. 2022;17:1–18. https://doi.org/10.1371/journal.pone.0259190.
48. Vanheuverzwijn J, Maillard EE, Mahat A, Fowler L, Monteyne D, Bonnaud L, et al. Easy, flexible and standardizable anti-nascent biofilm activity assay to assess implant materials. Microorganisms. 2023. https://doi.org/10.3390/microorganisms11041023.
49. EL-Moslamy SH, Elnouby MS, Rezk AH, El-Fakharany EM. Scaling-up strategies for controllable biosynthetic ZnO NPs using cell free-extract of endophytic *Streptomyces albus*: characterization, statistical optimization, and biomedical activities evaluation. Sci Rep. 2023;13:1–22. https://doi.org/10.1038/s41598-023-29757-9.
50. Shehabeldine AM, Amin BH, Hagras FA, Ramadan AA, Kamel MR, Ahmed MA, et al. Potential antimicrobial and antibiofilm properties of copper oxide nanoparticles: time-kill kinetic essay and ultrastructure of pathogenic bacterial cells. Appl Biochem Biotechnol. 2022. https://doi.org/10.1007/s12010-022-04120-2.
51. Loo YY, Rukayadi Y, Nor-Khaizura MAR, Kuan CH, Chieng BW, Nishibuchi M, et al. In vitro antimicrobial activity of green synthesized silver nanoparticles against selected Gram-negative foodborne pathogens. Front Microbiol. 2018;9:1–7. https://doi.org/10.3389/fmicb.2018.01555.
52. Mirmajidi T, Chogan F, Rezayan AH, Sharifi AM. In vitro and in vivo evaluation of a nanofiber wound dressing loaded with melatonin. Int J Pharm. 2021;596:120213. https://doi.org/10.1016/j.ijpharm.2021.120213.
53. El-Dakroury WA, Salim SA, Said AR, Asaad GF, Abdelhameed MF, Shabana ME, et al. Novel repurposing of Empagliflozin-loaded buccal composite (Chitosan/Silk Fibroin/Poly(lactic acid)) nanofibers for Alzheimer's disease management via modulation

of Aβ–AGER–p-tau pathway. Pharmaceutics. 2026;18:83. https://doi.org/10.3390/pharmaceutics18010083.
54. Süntar I, Küpeli Akkol E, Keles H, Yesilada E, Sarker SD. Exploration of the wound healing potential of *Helichrysum graveolens* (Bieb.) Sweet: isolation of apigenin as an active component. J Ethnopharmacol. 2013;149:103–10. https://doi.org/10.1016/j.jep.2013.06.006.
55. C.K. Mishra, A.K. Pattnaik, P. Dagur, D. Kumar, M. Ghosh, Excision and incision wound healing activity of apigenin (4', 5, 7-trihydroxyflavone) containing extracts of Carissa carandas Linn. fruits, Pharmacogn. Mag. 18 (2022).
56. Ghaisas MM, Kshirsagar SB, Sahane RS. Evaluation of wound healing activity of ferulic acid in diabetic rats. Int Wound J. 2014;11:523–32. https://doi.org/10.1111/j.1742-481X.2012.01119.x.
57. Bairagi U, Mittal P, Singh J, Mishra B. Preparation, characterization, and in vivo evaluation of nano formulations of ferulic acid in diabetic wound healing. Drug Dev Ind Pharm. 2018;44:1783–96. https://doi.org/10.1080/03639045.2018.1496448.
58. Bouzabata A, Montoro P, Gil KA, Piacente S, Youssef FS, Al Musayeib NM, et al. HR-LC-ESI-Orbitrap-MS-based metabolic profiling coupled with chemometrics for the discrimination of different *Echinops spinosus* organs and evaluation of their antioxidant activity. Antioxidants. 2022. https://doi.org/10.3390/antiox11030453.
59. El-Din MIG, George MY, Youssef FS. Chemical characterization of the polyphenolic rich fraction of *Thunbergia erecta* and its therapeutic potential against doxorubicin and cyclophosphamide-induced cognitive impairment in rats. J Ethnopharmacol. 2023. https://doi.org/10.1016/j.jep.2023.116213.
60. Abdelghffar EA, El-Nashar HAS, Al-Mohammadi AGA, Eldahshan OA. Orange fruit (*Citrus sinensis*) peel extract attenuates chemotherapy-induced toxicity in male rats. Food Funct. 2021;12:9443–55. https://doi.org/10.1039/d1fo01905h.
61. El-Nashar HAS, Abbas H, Zewail M, Noureldin MH, Ali MM, Shamaa MM, et al. Neuroprotective effect of Artichoke-based nanoformulation in Sporadic Alzheimer's disease mouse model: focus on antioxidant, anti-inflammatory, and amyloidogenic pathways. Pharmaceuticals. 2022;15:1202. https://doi.org/10.3390/ph15101202.
62. Zengin G, Fahmy NM, Sinan KI, Uba AI, Bouyahya A, Lorenzo JM, et al. Differential metabolomic fingerprinting of the crude extracts of three Asteraceae species with assessment of their in vitro antioxidant and enzyme-inhibitory activities supported by in silico investigations. Processes. 2022;10:1911. https://doi.org/10.3390/pr10101911.
63. Hamdan DI, Salah S, Hassan WHB, Morsi M, Khalil HMA, Ahmed-Farid OAH, et al. Anticancer and neuroprotective activities of ethyl acetate fractions from *Morus macroura* Miq. plant organs with ultraperformance liquid chromatography-electrospray ionization-tandem mass spectrometry profiling. ACS Omega. 2022. https://doi.org/10.1021/acsomega.2c01148.
64. Kadhim HM, Hamad MN, Kadhim YM. Isolation and identification of two cucurbitacins B and E, and detection of phytosterols in *cucurbita pepo* L. var. pepo (pumpkin) leaves extract. Int J Drug Deliv Technol. 2020;10:369–73. https://doi.org/10.25258/ijddt.10.3.11.
65. Abdelazim E, Goher S, Aly S, El-Nashar H, EL-Moslamy S, El-Fakharany E, et al. In vitro and in vivo studies of *Syzygium cumini* loaded electrospun PLGA/PMMA/collagen nanofibers for accelerating topical wound healing. RSC Adv. 2024;14:101–17.
66. Kulczynski B, Gramza-Michałowska A. The profile of secondary metabolites and other bioactive compounds in *cucurbita pepo* L. and *cucurbita moschata* pumpkin cultivars. Molecules. 2019. https://doi.org/10.3390/molecules24162945.
67. M. Terzic, S. Fayez, N.M. Fahmy, O.A. Eldahshan, A.I. Uba, S.K.M. Ponniya, S. Selvi, Nilofar, I. Koyuncu, Ö. Yüksekdağ, G. Zengin, Chemical characterization of three different extracts obtained from Chelidonium majus L. (Greater celandine) with insights into their in vitro, in silico and network pharmacological properties, Fitoterapia 174 (2024). https://doi.org/10.1016/j.fitote.2024.105835.
68. AbouZeid EM, Afifi AH, Salama A, Hussein RA, Youssef FS, El-Ahmady SH, et al. Comprehensive metabolite profiling of *Phoenix rupicola* pulp and seeds using UPLC-ESI-MS/MS and evaluation of their estrogenic activity in ovariectomized rat model. Food Res Int. 2022. https://doi.org/10.1016/j.foodres.2022.111308.
69. Choi HW, Woo HJ, Hong W, Kim JK, Lee SK, Eum CH. Structural modification of poly(methyl methacrylate) by proton irradiation. Appl Surf Sci. 2001;169:433–7. https://doi.org/10.1016/S0169-4332(00)00699-1.
70. SachinParmar NSD, Gangwal A. FT-IR and FT-Raman spectra and normal coordinate analysis of poly methyl methacrylate. Scholars Research Library. 2011;2:373–83.
71. Madejová J, Gates WP, Petit S. IR Spectra of Clay Minerals. In: Dev. Clay Sci. 2017. p. 107–49. https://doi.org/10.1016/B978-0-08-100355-8.00005-9.
72. Cheng H, Frost RL, Yang J, Liu Q, He J. Infrared and infrared emission spectroscopic study of typical Chinese kaolinite and halloysite. Spectrochim Acta A Mol Biomol Spectrosc. 2010;77:1014–20. https://doi.org/10.1016/j.saa.2010.08.039.
73. Hu D, Si WB, Qin W, Jiao J, Li XL, Gu XP, et al. *Cucurbita pepo* leaf extract induced synthesis of zinc oxide nanoparticles, characterization for the treatment of femoral fracture. J Photochem Photobiol B. 2019;195:12–6. https://doi.org/10.1016/j.jphotobiol.2019.04.001.
74. Grzybek M, Kukula-Koch W, Strachecka A, Jaworska A, Phiri AM, Paleolog J, et al. Evaluation of anthelmintic activity and composition of pumpkin (*Cucurbita pepo* L.) seed extracts—in vitro and in vivo studies. Int J Mol Sci. 2016. https://doi.org/10.3390/ijms17091456.
75. El Khatib LW, Rahal HT, Abdel-Gaber AM. Synergistic effect between *Fragaria ananassa* and *Cucurbita pepo* L leaf extracts on mild steel corrosion in hydrochloric acid solutions. Protection of Metals and Physical Chemistry of Surfaces. 2020;56:1096–106. https://doi.org/10.1134/S2070205120050111.
76. Le Ba T, Alkurdi AQ, Lukács IE, Molnár J, Wongwises S, Gróf G, et al. A novel experimental study on the rheological properties and thermal conductivity of halloysite nanofluids. Nanomaterials. 2020;10:1–14. https://doi.org/10.3390/nano10091834.
77. Salim SA, Kamoun EA, Evans S, El-Moslamy SH, El-Fakharany EM, Elmazar MM, et al. Mercaptopurine-loaded sandwiched trilayered composed of electrospun polycaprolactone/poly (methyl methacrylate) nanofibrous scaffolds as anticancer carrier with antimicrobial and antibiotic features: sandwich configuration nanofibers, release study and in vitro bioevaluation tests. Int J Nanomedicine. 2021. https://doi.org/10.2147/ijn.s332920.
78. Malik S, Muhammad K, Waheed Y. Nanotechnology: a revolution in modern industry. Molecules. 2023. https://doi.org/10.3390/molecules28020661.
79. Makabenta JMV, Nabawy A, Li C-H, Schmidt-Malan S, Patel R, Rotello VM. Nanomaterial-based therapeutics for antibiotic-resistant bacterial infections. Nat Rev Microbiol. 2021;19:23–36. https://doi.org/10.1038/s41579-020-0420-1.
80. Strodtbeck F. Physiology of wound healing. Newborn Infant Nurs Rev. 2001;1:43–52. https://doi.org/10.1053/NBIN.2001.23176.

Publisher's Note Springer Nature remains neutral with regard to jurisdictional claims in published maps and institutional affiliations.